

**Global Ocean Surface Velocities from Drifters: Mean, Variance, ENSO Response,
and Seasonal Cycle**

Rick Lumpkin¹ and Gregory C. Johnson²

for *Journal of Geophysical Research–Oceans*

Submitted 24 September 2012

Revised 19 April 2013

¹NOAA/Atlantic Oceanographic and Meteorological Laboratory, 4301 Rickenbacker
Causeway, Miami FL 33149 USA

²NOAA/Pacific Marine Environmental Laboratory, 7600 Sand Point Way NE Bldg. 3,
Seattle WA 98115 USA

e-mail: Rick.Lumpkin@noaa.gov

This article has been accepted for publication and undergone full peer review but has not been through the copyediting, typesetting, pagination and proofreading process which may lead to differences between this version and the Version of Record. Please cite this article as doi: 10.1002/jgrc.20210

ABSTRACT

Global near-surface currents are calculated from satellite-tracked drogued drifter velocities on a $0.5^\circ \times 0.5^\circ$ latitude-longitude grid using a new methodology. Data used at each grid point lie within a centered bin of set area with a shape defined by the variance ellipse of current fluctuations within that bin. The time-mean current, its annual harmonic, semiannual harmonic, correlation with the Southern Oscillation Index (SOI), spatial gradients, and residuals are estimated along with formal error bars for each component. The time-mean field resolves the major surface current systems of the world. The magnitude of the variance reveals enhanced eddy kinetic energy in the western boundary current systems, in equatorial regions, and along the Antarctic Circumpolar Current, as well as three large “eddy deserts”, two in the Pacific and one in the Atlantic. The SOI component is largest in the western and central tropical Pacific, but can also be seen in the Indian Ocean basin. Seasonal variations reveal details such as the gyre-scale shifts in the convergence centers of the subtropical gyres and the seasonal evolution of tropical currents and eddies in the western tropical Pacific Ocean. The results of this study are available as a monthly climatology.

1. Introduction

Knowledge of global near-surface currents is important for a variety of uses including ship routing, search and rescue efforts, biological and chemical studies, and both hindcasts and forecasts of the transport and dispersion of floating material including plastic and oil [c.f., *McCord et al.*, 1999; *Davidson et al.*, 2009; *Yoder et al.*, 1994; *Law et al.*, 2010; *Maximenko et al.*, 2012]. Here we apply a new methodology to derive the global distribution of time-mean near-surface ocean currents, their seasonal cycle, their projection onto the Southern Oscillation Index (ENSO), and the variance of eddy fluctuations from a homogeneous data set of global near-surface current observations from the satellite-tracked drifters of the Global Drifter Program (GDP) [*Niiler*, 2001; *Lumpkin and Pazos*, 2007].

Although previous studies have derived a global mean surface velocity field from GDP drifter observations [c.f., *Maximenko et al.*, 2009], they have suffered from contamination by undiagnosed drogue loss for a significant fraction of the data [*Grodsky et al.*, 2011; *Rio et al.*, 2011]. GDP drifters have a drogue (sea anchor) centered at a depth of 15 m to reduce the downwind slip (motion with respect to the current at 15 m depth) to ~0.1% of the wind speed for winds up to 10 m s^{-1} [*Niiler et al.*, 1995] and follow the water within the mixed layer. When this drogue is lost, the downwind slip increases to ~1–1.5% of the wind speed [*Pazan and Niiler*, 2001; *Poulain et al.*, 2009; *Lumpkin et al.*, 2012]. A recent reanalysis of drogue presence has removed undrogued data from the GDP data set [*Lumpkin et al.*, 2012]. Here we set out a new method for binning and mapping the data that captures spatial and temporal variations in the data and

produces formal error bars for the mapped velocity components. These results are made available at http://www.aoml.noaa.gov/phod/dac/dac_meanvel.php.

2. Data and Methods

This analysis uses quality controlled data from the GDP from 1979 through June 2012, interpolated via kriging to regular 6-hour intervals [*Hansen and Poulain, 1996*].

Velocities every 6 hours are obtained via 12-hour centered differencing of the kriged positions. Recent analyses have found a significant fraction of the velocities in the time period 2002–2009 previously believed to be from drogued drifters were from undrogued drifters; in this study, only data from drogued drifters are used, following results of a manual reevaluation of drogue presence [*Lumpkin et al., 2012*]. NCEP operational 6-hour surface (0.995 sigma level) winds W are interpolated to the drifter locations and a downwind slip of $7 \times 10^{-4} W$ [*Niiler and Paduan, 1995*] is removed from the remaining drifter velocities. The resulting velocities are lowpassed with a 2-point Butterworth filter with half-power cutoff at five days to remove tidal and near-inertial components of the flow, then decimated to daily values for this analysis. No attempt is made to separate Ekman and geostrophic velocities [e.g., *Lumpkin and Garzoli, 2005*].

Following *Johnson [2001]*, zonal and meridional drifter speeds are mapped in elliptical bins centered on a $0.5^\circ \times 0.5^\circ$ longitude-latitude grid, with the ratio of semi-major to semi-minor axis and axis orientation set by the variance ellipse of eddy fluctuations (residuals with respect to the mapped current within the bin; see below) in the bin. For this study we chose bins with an area equal to that of an ellipse with radii of 2° (i.e., area = $\pi \times 2^\circ \text{ lat.} \times 2^\circ \text{ long.}$). Hence the bin area at $\pm 60^\circ$ latitude is half that at the equator

owing to the reduction of the zonal radius with increasing latitude, reflecting, albeit only weakly, the reduction of the Rossby radius of deformation at high latitudes [e.g., *Chelton et al.*, 1998], and its influence in reducing ocean current scales at higher latitudes [e.g., *Stammer et al.*, 2007]. The bin area is chosen subjectively to balance resolution of known current features while limiting aliased short-term variability in the maps. Other bin areas were tested but found to be less optimal for global application: for example, bins of half the area better resolved fine-scale currents in well-sampled regions of flow/topography interaction such as the Hawaiian Islands, but these small bins also tended to produce spurious features likely reflecting undersampled realizations of the time-varying mesoscale field in poorly-sampled regions. Alternatively, bins of twice the area were superior for resolving large-scale currents in poorly-sampled regions, but overly smoothed features of the time-mean field (such as the Loop Current) that had converged at the resolution we chose. There are other possible choices for binning the data such as orienting bins along planetary potential vorticity contours [e.g., *Jacobsen et al.*, 2003] or the application of clustering methods to improve Lagrangian statistics [e.g., *Koszalka et al.* 2011]. Our choice is relatively simple, dynamically motivated, and homogeneously applied around the globe, and results in a uniformly-gridded product.

Within each bin, the complex vector \mathbf{u} containing observations $u + iv$ of zonal u and meridional v drifter speed can be written $\mathbf{u} = \mathbf{A}\mathbf{z} + \mathbf{u}'$, where \mathbf{u}' are residuals (eddy fluctuations), \mathbf{z} is a vector containing 11 coefficients to be determined, and matrix \mathbf{A} describes the model used to map the large-scale currents:

$$\mathbf{A}_j = [1 \quad SOI_j \quad \sin(2\pi t_j) \quad \cos(2\pi t_j) \quad \sin(4\pi t_j) \quad \cos(4\pi t_j) \quad x_j \quad x_j^2 \quad y_j \quad y_j^2 \quad x_j y_j]. \quad (1)$$

Here the subscript j indicates observation j collected at time t_j (in years). The unity term models the time mean. The term SOI_j is a running five-month average of the Southern Oscillation Index [Trenberth, 1984] centered at t_j ; this term models the influence of ENSO, and is especially important near the equator, where drifter observations may be biased towards El Niño-related periods of weak Trade Winds and associated low equatorial divergence [Johnson, 2001]. We include the SOI because it is generally well sampled over multiple cycles by the drifter data and is associated with strong variations in surface currents, especially across the tropical Pacific [e. g. Johnson et al., 2002]. The GDP-style drifters were deployed in their first decade of existence (1979–1989) almost solely in the tropical Pacific, motivated by the desire to resolve ENSO-related climate fluctuations. As noted by Johnson [2001], the SOI is correlated with the strength of Pacific equatorial divergence and thus surface drifter observational density, and can thus be expected to bias time-mean calculations if a SOI component is not included. We do not include other climate indices, such as the North Atlantic Oscillation [Hurrell, 1995], Pacific Decadal Oscillation [Mantua et al., 1997], or Antarctic Oscillation [Thompson and Wallace, 2000] because the data generally do not span all phases of these indices in as large a fraction of the bins, so they would not be well fit. However, as data records become longer, including such indices in future models might improve the results, which may be biased now towards one phase or the other of these phenomena. The sinusoidal terms fit annual and semi-annual harmonics [Johnson, 2001; Lumpkin, 2003]. The use of only two harmonics may not resolve the seasonal cycle fully everywhere, but it keeps the number of parameters in the model relatively low. This approach has been used previously and successfully with sparsely sampled, inhomogenous oceanographic data

sets [e.g., *Ridgeway et al.*, 2002]. The final five terms in A_j model spatial gradients within the bin [*Bauer et al.*, 1998; *Johnson*, 2001] and are expressed with respect to the non-dimensionalized zonal distance x_j and meridional distance y_j from the bin center, expressed in degrees longitude or latitude divided by 1° .

While a simultaneous fit to 11 coefficients is superior to a stepwise approach if all coefficients can be resolved by the data [c.f., *Lumpkin*, 2003], spurious results can result in bins with low observational density, particularly those that also have energetic mesoscale fluctuations. Examining results from the 11-coefficient fit as a function of observational density outside the tropical Pacific, we find that spuriously large results for the SOI coefficient are calculated in bins with < 365 drifter-days of observations (corresponding to 29 drifter-days per square degree). Comparable results are found for the seasonal sinusoid coefficients with < 90 drifter-days of observations. In bins with < 365 drifter-days, the SOI term is not included in the model (1); in bins with < 90 drifter-days, the seasonal sinusoid terms are not included. If there are < 10 drifter-days of data (i.e., 2–3 Lagrangian integral time scales) then the calculation is not made and the bin is left blank.

The model is evaluated iteratively, starting with a circular bin, and calculating the resulting variance ellipses to determine a new ellipsoidal bin and new model coefficients [c.f., *Johnson*, 2001]. The calculation is iterated a total of five times for each bin to ensure convergence.

The Gauss-Markov estimator for z in a given bin is

$$z = \mathbf{R}_z \mathbf{A}^T (\mathbf{A} \mathbf{R}_z \mathbf{A}^T + \mathbf{R}_n)^{-1} \mathbf{u}, \quad (2)$$

[c.f., Wunsch, 1996; Lumpkin, 2003], where \mathbf{R}_z is the *a priori* (calculated before solving for \mathbf{z}) covariance matrix of the unknown coefficients in \mathbf{z} and \mathbf{R}_n is the variance structure of the eddy noise \mathbf{u}' . For this study each of the diagonal elements of \mathbf{R}_z are assumed to be equal to the range of $|\mathbf{u}^2|$ and off-diagonal elements are set to zero. In principle prior knowledge could guide the values of the terms in \mathbf{R}_n ; our choice to set them all equal assumes that any term in (1) could potentially account for the observed variance of \mathbf{u} in each bin. Elements of \mathbf{R}_n are chosen to be

$$R_n(\tau)=[\text{std}(u)^2 + i \text{std}(v)^2] \cos(\pi\tau / 2T_d) \exp[-(\pi\tau / 2\sqrt{2} T_d)^2] \quad (3)$$

following Lumpkin [2003], with $T_d=10.33$ days, consistent with an integral eddy time scale of five days. This choice assigns degrees of freedom to the observations with the assumption that observations less than five days apart are not fully independent [Lumpkin, 2003], a conservative choice since many studies have found values of 2–3 days for the integral time scale. The *a posteriori* error covariance matrix is

$$\mathbf{P}_z = \mathbf{R}_z - \mathbf{R}_z \mathbf{A}^T (\mathbf{A} \mathbf{R}_z \mathbf{A}^T + \mathbf{R}_n)^{-1} \mathbf{A} \mathbf{R}_z \quad (4)$$

[c.f., Wunsch, 1996]. The square roots of the diagonal terms in \mathbf{P}_z are the formal error bars for the coefficients in \mathbf{z} ; for example, $[\mathbf{P}_z(1,1)]^{0.5}$ is the error for time-mean \mathbf{u} at the bin center. Since fitting multiple parameters at once can sometimes lead to spurious results, these error bars can be examined at any location to assess how well the various terms in the model are resolved. The total squared error for the mapped speed $\mathbf{A}\mathbf{z}$ is $\mathbf{A}\mathbf{P}_z\mathbf{A}^T$. This quantity can, for example, be used to derive error bars on seasonal or monthly mean values. The magnitudes of the coefficients \mathbf{z} and the residuals \mathbf{u}' are compared against the prior values (square roots of the diagonal terms in \mathbf{R}_z and \mathbf{R}_n ,

respectively) in each bin. The solution in a bin is rejected if $|z|$ exceeds the prior value in R_z or if more than 40% of the residuals exceeds the prior value in R_n .

The number of daily observations within each bin is highly inhomogeneous (Figure 1), being a function of deployment locations and the subsequent advection pathways, including regions of divergence and convergence that impact drifter residence times. Regions of poor data coverage (< 50 drifter days per square degree) are located in the southernmost Southern Ocean, the southeast Pacific Ocean west of Chile, the Southern Ocean south of Australia, the southwest Pacific immediately north of New Zealand, the western equatorial Indian Ocean, the central equatorial Atlantic Ocean, the easternmost Angola Basin, and the Java Sea (much of which is shallower than 15 m).

The data are also not homogeneous in time: the earliest deployments (in 1979) were conducted solely in the tropical Pacific Ocean as part of the Tropical Ocean Global Atmosphere study [Niiler, 2001]. Sustained deployments began in the North Atlantic in 1989 [Fratantoni, 2001], the South Atlantic in 1993, the Indian Ocean in 1994, and the Tropical Atlantic in 1997 [Lumpkin and Garzoli, 2005]. From 1993–2002, the array averaged 500–700 drifters at any given time; it was increased to its current size of ~1250 drifters in late 2005 and has been subsequently sustained at approximately this size [Lumpkin and Pazos, 2007].

3. Results

We start with a presentation of the mean speed and streamlines as well as variance ellipses. We then discuss the regression of surface currents onto the SOI. Following that, we present the global seasonal cycle of the surface currents. As examples of the details

visible in the climatology, we discuss the seasonal cycle of surface currents in the western tropical Pacific Ocean and the surface divergence fields of the equatorial interior ocean basins. We conclude with a comparison to an oft-used surface current product.

3.1. Mean fields

Unsmoothed mean current speeds (to indicate local current magnitudes) with streamlines calculated from spatially smoothed velocities (to indicate large-scale interior current directions as well as qualitatively, the surface divergence field) clearly illustrate the prominent large-scale currents (Figure 2) such as the western boundary currents, their extensions, the equatorial current systems, and parts of the Antarctic Circumpolar Current (ACC). Only the streamlines are computed from smoothed fields, which do attenuate some smaller-scale regional features, with all other quantities displayed as mapped. The smoothing is applied only to bins with mean speeds $< 25 \text{ cm s}^{-1}$ so that strong currents are not smoothed, while spurious localized convergences and divergences in regions of weak velocity are reduced. This smoothing is an average of the grid value and eight surrounding values, weighted by observational density, iterated 10 times to stress the large-scale field. The global histogram of unsmoothed mean speeds (Figure 2, inset) peaks at $4.5\text{--}6 \text{ cm s}^{-1}$, with 87% of the bins having a mean speed $< 25 \text{ cm s}^{-1}$ and 98% $< 50 \text{ cm s}^{-1}$.

3.1.1 Prominent currents

The features of prominent regional surface current systems discussed below are visible in the drifter-derived velocity fields, but may be difficult to see in the global-scale

maps presented in this paper. Maps of specific current systems derived from our results can be seen at <http://oceancurrents.rsmas.miami.edu/> or can be generated from the climatology, available at http://www.aoml.noaa.gov/phod/dac/dac_meanvel.php.

The structure of the Antarctic Circumpolar Current (ACC) is resolved as strong jets associated with the Southern Ocean fronts, surrounded by regions of relatively weak flow [Orsi *et al.*, 1995; Falco and Zambianci, 2011]. The ACC bifurcates east of the Drake Passage (Figure 2), with a significant portion flowing north in the western Atlantic as the Malvinas Current, perhaps the equivalent of the western boundary for this otherwise zonally unbounded current [e.g., Baker, 1982]. After meeting the southward-flowing Brazil Current at the Brazil/Malvinas Confluence, the South Atlantic Current continues eastward across the South Atlantic and enters the southern Indian Ocean basin. Paralleling this to the south, the southern fronts of the ACC enter the Indian Ocean sector and slowly migrate southward as they flow eastward through the Indian and Pacific sectors [e.g., Orsi *et al.*, 1995; Falco and Zambianci, 2011], distinct at some longitudes, merged at others in this climatology. The ACC is narrower and in some areas up to 10 cm s^{-1} weaker than in previous mean current fields calculated from drifters prior to the recent drogoue presence reassessment [Lumpkin *et al.*, 2013], and perhaps also affected by changes in mapping methods. The ACC is not resolved in the central and eastern South Pacific owing to the scarcity of drogued data in this region.

In the northern and equatorial Indian Ocean, with its strong seasonal cycle [e.g., Schott and McCreary, 2001], discussed below, the time-mean surface currents (Figure 2) are dominated by the northward-flowing Somali western boundary current and eastward equatorial Wyrтки Jet. In the Indian Ocean, the westward-flowing South Equatorial

Current (SEC) at 24–6.5°S is shifted further south than in the other oceans, with a maximum speed of 20–24 cm s⁻¹ at 12°S. The SEC is fed in part by the Indonesian Throughflow [Gordon *et al.*, 1997]. In the surface layer it bifurcates near 16°S upon reaching Madagascar, with the northern branch heading westward to Africa and then turning northward to join the East Africa Current [e.g., Swallow *et al.*, 1988]. The fate of the southern branch of the East Madagascar Current when it reaches the southern end of Madagascar is less clear [e.g., Lutjeharms, 2007], but in the mean drifter climatology it appears to form a jet extending west-southwest from the southern tip of Madagascar to 28°S, 40°W. This jet then splits, with one branch flowing southward to join the Agulhas return current and the other flowing westward to join with the southward-flowing Mozambique Current to feed the Agulhas Current. The Agulhas has time-mean speeds of 60–150 cm s⁻¹, with the greatest speeds found from 32.5°S, 29°E to 34.5°S, 25.5°E. The Agulhas retroflects south of Africa, at 20–23°E in the mean — a bit further to the east than expected [e.g., Lutjeharms, 2007] — to feed the eastward-flowing South Indian Ocean Current which exhibits prominent meanders as it flows eastward to ~45°E and then east-southeastward to merge eventually with the ACC. On the east side of the Indian Ocean, the Leeuwin Current flows south along the west coast of Australia [Feng *et al.*, 2003], with a speed of 20–35 cm s⁻¹ in the latitude band 24–26.5°S, but it appears in the mean to be interrupted by an apparently permanent anti-cyclonic feature centered at ~29°S, 111°E; northward currents on the west side of this feature oppose the Leeuwin Current and reduce its strength. South of 30°S the Leeuwin Current exceeds 100 cm s⁻¹ in several bins. It wraps around the southwest corner of Australia and continues eastward along Australia's south coast.

In the North Pacific, the Alaskan Stream [Reed, 1984] is apparent in the mean surface velocity from the drifter data (Figure 2) just south of Alaska and the Aleutian Island chain, petering out by about 170°E after it leaves its effective western boundary, near the dateline, where the island chain curves back to the northwest. The southward-flowing East Kamchatka Current and Oyashio, the western boundary currents of the subpolar gyre, are less prominent than the northward-flowing Kuroshio of the subtropical gyre, as is their eastward-flowing extension [e.g., Qu *et al.*, 2001], which slows to eastward speeds $<10 \text{ cm s}^{-1}$ by 170°W.

The equatorial Pacific currents are prominent in the mean drifter velocities (Figure 2), with the westward flowing North Equatorial Current (NEC) at 9–24°N attaining a peak speed of 20 cm s^{-1} at 11°N when averaged in the zonal band 150°E–140°W. The NEC extends from about 120°W to the Philippines, where it bifurcates to feed the northward-flowing Kuroshio and the southward flowing Mindanao Current [e.g., Toole *et al.*, 1990]. The Costa Rica Dome stands out as a small isolated anti-cyclonic circulation centered near 9°N, 95°W [Fiedler, 2002]. To the northwest, a region of anti-cyclonic circulation at 12–16°N, 106–95°W may be the rectified signature of the wind-generated anti-cyclonic Tehuantepec and Papagayo eddies which are generated in this region from October to July [Palacios and Bograd, 2005]. In the monthly mean velocity fields (not shown), the eastward flow in the northern half of this region is weakest in August–September, while the westward flow in the southern half is weakest in May–June. The North Equatorial Countercurrent (NECC) extends all the way across the Pacific [e.g., Johnson *et al.*, 2002]. In the Pacific the SEC is strongest at very low latitudes, with a narrow, $\sim 45 \text{ cm s}^{-1}$ (averaged from 180–100°W) branch at 2°N and a

larger branch of maximum speed $30\text{--}35\text{ cm s}^{-1}$ centered at 4°S at $140\text{--}110^{\circ}\text{W}$ that gradually shifts northward as it flows west, reaching 2°S by the dateline. These branches are separated by eastward surface flow at the equator in the central to eastern Pacific (the shoaled equatorial undercurrent) [Johnson *et al.*, 2002]. This feature is apparent in the unsmoothed maps, but absent in the streamlines, which are computed after smoothing the maps. The SEC is also strong along about 15°S from the dateline into the Coral Sea, where it bifurcates at the east coast of Australia, with part heading north towards the equator via the Solomon Sea (again, not visible in the smoothed streamlines) and the New Guinea Coastal Current and another portion feeding the southward flowing East Australia Current [e.g., Ganachaud *et al.*, 2008] which has a peak speed of 90 cm s^{-1} at 30.5°S , 153.5°E .

In the subpolar North Atlantic Ocean, the $30\text{--}35\text{ cm s}^{-1}$ East Greenland Current rounds Cape Farewell (Fig. 2; visible in the current speeds) to become the west Greenland current with peak speeds of $45\text{--}50\text{ cm s}^{-1}$, and then the $15\text{--}30\text{ cm s}^{-1}$ Labrador Current, before meeting the Gulf Stream extension near Newfoundland [e.g., Higginson *et al.*, 2011]. The northward-flowing Norwegian Atlantic Current is also prominent in the drifter data [e.g., Jakobsen *et al.*, 2003; Koszalka *et al.*, 2011]. The return currents in the gyre interior are discussed below.

In the southwestern tropical Atlantic, the North Brazil Current [Garzoli *et al.*, 2004; Lumpkin and Garzoli, 2005] bifurcates, with the western portion, the Guyana Current [c.f., Richardson and Walsh 1986], entering the Caribbean to form the $30\text{--}50\text{ cm s}^{-1}$ Caribbean Current, which passes north of a clearly defined (Figure 2; visible in the current speeds) Columbia-Panama gyre in the southern Columbia Basin [c.f., Richardson,

2005]. The Caribbean Current feeds into the Yucatan Current, which in turn feeds the high-speed Loop Current in the Gulf of Mexico [c.f., *Molinari and Morrison*, 1988], which in turn joins the Gulf Stream flowing north to Cape Hatteras. In the time-mean the Gulf Stream is 70–80 cm s⁻¹, with speeds exceeding 90 cm s⁻¹ in the Florida Current and at its separation from the coast near Cape Hatteras. The Gulf Stream splits to the northeast to feed the North Atlantic Current [e.g., *Schmitz and McCartney*, 1993] and to the southeast to return to the subtropical Gyre. The North Atlantic Current in turn splits to feed the North Atlantic Drift that returns to the subpolar gyre, and the Azores Current [e.g., *Klein and Siedler*, 1989] that eventually feeds the equatorward eastern boundary flow and upwelling regime associated with the Canary Current [e.g., *Mason et al.*, 2012].

The tropical Atlantic mean circulation (Figure 2) is dominated by a zonally elongated clockwise gyre consisting of the westward northern and central branches of the SEC, the northwestward North Brazil Current (NBC) and its southeastward retroflexion, and the eastward NECC and Guinea Current [*Lumpkin and Garzoli*, 2005]. Very large time-mean speeds of 80–140 cm s⁻¹ are found in the NBC, with the largest speeds located at 4–7°N, 54–50°W immediately before the NBC splits into the southeastward Retroflexion and the westward Guyana Current. Upwelling and cross-equatorial flow of surface waters evident in the mean surface drifter climatology play a role in the warm return flow of the Atlantic Meridional Overturning Circulation [e.g., *Roemmich*, 1981].

In the South Atlantic, the surface expression of the southern SEC (Figure 2) bifurcates against the South American coast at 14–14.5°S to form the north-northeastward NBC and the south-southwestward Brazil Current [e.g., *Rodrigues et al.*, 1999]. The Brazil Current meets the north-northeastward Malvinas Current at 37°S,

54°W in the time-mean at the surface. The Brazil-Malvinas Confluence is a complex, energetic region [e.g., *Provost et al.*, 1992, *Lumpkin and Garzoli*, 2011]; in the mean drifter climatology the Malvinas Current has speeds of 30–50 cm s⁻¹ against the South American shelf, with comparable speeds in the southward Brazil/Malvinas Confluence jet, which extends south to about 45°S. The eastward flow emerging from the Confluence region is strongest at 48°S, associated with the Subpolar Front, with a secondary jet at 40°S associated with the Subtropical Front [*Orsi et al.*, 1995].

3.1.2 Interior gyres, convergence, and divergence.

Global streamlines converge in the centers of the subtropical gyres, associated with the convergent subtropical fronts (Figure 2). These fronts terminate in “garbage patches” in both hemispheres of the eastern (centered near 35°N, 140°W and 30°S, 100°W) Pacific and the eastern (25°S, 100°E) South Indian oceans [*Maximenko et al.*, 2012; *van Sebille et al.*, 2012]. These locations are characterized by high concentrations of floating plastics and other debris. In the Atlantic the convergences are centered further to the west (near 30°N, 50°W and 30°S, 25°W) [e.g., *Law et al.*, 2011]. In contrast, streamlines diverge from the subpolar gyres of the North Pacific and North Atlantic. Subpolar divergence south of the ACC, where deep water is upwelled [e.g., *Sloyan and Rintoul*, 2001], is not resolved by the drifters.

Divergence from the equatorial Pacific and Atlantic is also extremely prominent (Figure 2), and is associated with the cold tongues of upwelled water from below [e.g., *Johnson et al.*, 2001; *Grodsky and Carton*, 2002]. However, in the equatorial Indian Ocean, acceleration of the flow across the equator is consistent with weaker horizontal

divergence (see Section 3.3) that is not as visually apparent as in the equatorial Pacific and Atlantic. In fact, there is a net southward surface flow observed at the equator, closing a mean cell of subducted water in the Southern Hemisphere and upwelled water in the North [Schott *et al.*, 2004]. Divergence is apparent near 8°S in the western tropical Indian Ocean, where the winds bring the thermocline close to the surface [e.g., *Hermes and Reason*, 2008], as well as in the Costa Rica Dome near 9°N, 90°W [Fiedler, 2002].

Streamlines also clearly diverge from the west coasts of North and South America and Africa (apart from the latitude band of the NECC, Figure 2), where the equatorward-flowing eastern boundary currents are associated with coastal upwelling [e.g., *Bograd et al.*, 2009; *Colas et al.*, 2012; *Hutchings et al.*, 2009; *Nyckær and Van Camp*, 1994]. In contrast, the streamlines do not indicate divergence along the Australian west coast, where the poleward-flowing Leeuwin Current (visible in the current speeds) carries warm water southward, and the winds and circulation inhibit upwelling [Feng *et al.*, 2003].

3.2 Variance

The mean speed of eddy fluctuations with respect to the model fit (i.e., fluctuations with respect to the time-mean, seasonal, and SOI-related variations, equal to the square root of twice the eddy kinetic energy) shows large geographic variations (Figure 3). These results are comparable to those from satellite altimetry [e.g., *Ducet et al.*, 2000], except that the surface drifter analysis can be carried to the equator as geostrophy need not be assumed. Maximum eddy speeds exceeding 70 cm s⁻¹ are found in the Somali Current region; values > 60 cm s⁻¹ are also found in the Gulf Stream and Agulhas Retroflexion, and > 50 cm s⁻¹ also in the Loop Current, Florida Current, the

Pacific NECC and northern SEC at 115–130°W (presumably associated with energetic Tropical Instability Waves), Kuroshio Current, Brazil/Malvinas Confluence, Agulhas Return Current, North Brazil Current Retroflexion, Mozambique Channel, and the East Australian Current. Enhanced eddy energy is also seen along the path of the ACC, west of the Hawaiian Islands, in the Pacific Subtropical Countercurrents, and along much of the NECCs of the Atlantic and Pacific basins.

In contrast, “eddy deserts” with time-mean eddy speeds $< 10 \text{ cm s}^{-1}$ dominate three large regions: the subtropical South Atlantic, the subpolar North Pacific, and the southeastern South Pacific ($\sim 110\text{--}85^\circ\text{W}$ from $40\text{--}10^\circ\text{S}$, and extending west to 170°W in the band $45\text{--}35^\circ\text{S}$). Much smaller eddy deserts are found in the central subtropical North Atlantic, west and south of New Zealand and south of the merged Agulhas Return Current and ACC immediately south of Kerguelen Island. Again, drifter speeds in this study have been lowpass filtered at 5 days; higher frequency motion may be present in these eddy deserts [Griffa *et al.*, 2008].

The variance ellipses for these eddy fluctuations (Figure 3) tend to align with most of the major currents such as the Gulf Stream and Kuroshio, although this tendency is less apparent in the East Australia and the Agulhas Return currents. Near the coasts, the ellipses tend to align with the coastlines. In the ocean interiors they are generally more circular, except at low latitudes, particularly in the Pacific and Indian equatorial bands, where they are zonally elongated. The coastal and equatorial waveguides are presumably largely responsible for these patterns.

3.3 Southern Oscillation Index (SOI) and surface currents

Current speeds and directions from the regression against the SOI (Figure 4, plotted for SOI = -1, corresponding to a moderate El Niño) contain the anticipated eastward (and slightly equatorially convergent) surge of surface currents in the Equatorial Pacific [e.g., *Johnson et al.*, 2000]. Eastward values of 10–20 cm s⁻¹ are seen in the equatorial Pacific (2°S–3°N) from 160°E to nearly 160°W, and along 155–110°W from 2–3°N. A weaker response mirroring the 2–3°N response is seen just south of the equator in the eastern tropical Pacific. East of 145°W, the response on the equator is not statistically significantly different from zero owing to the scarcity of observations (Figure 1). In the western tropical South Pacific there is another patch of anomalous westward flow associated with an El Niño-related shift in the South Pacific Convergence Zone [e.g., *Cai et al.*, 2012]. Curiously, the response in the Tehuantepec and Papagayo eddy region 12–15°N, 105–95°W suggests a weakening of the anti-cyclonic recirculation even though more frequent and stronger anti-cyclonic eddies are thought to be generated there during El Niños [*Palacios and Bograd*, 2005].

In the Indian Ocean, El Niño-related westward speeds of ~4–8 cm s⁻¹ can be found in a band stretching west-northwestward across the basin from ~12°S, 100°E to ~1°N, 50°E, generally increasing toward the west. There is another patch of westward flow just north of the equator south of India and Sri Lanka associated with El Niño. Strong (15–25 cm s⁻¹) southwestward anomalies against Somalia oppose the seasonal northeastward Somali Current north of 4°N during El Niño; SOI-related variations further south cannot be resolved due to observational densities of < 365 drifter days per bin. The large spatial extent and coherent directions in the features associated with El Niño discussed above suggest they may be robust. Other less spatially coherent patterns

include a slowing of the surface currents in the Gulf Stream, eastward flow in the deep section of the eastern Bering Sea, and westward flow in the Mediterranean Sea, all apparently during El Niño. However, these latter features, given their relatively small spatial extent and absence of documented teleconnection mechanisms, may simply result from spurious correlations with the SOI. There are isolated patches of response in other areas, but nothing aside from the patterns already discussed stands out as spatially coherent.

3.4. Seasonal variations

Monthly mean ocean currents for climatological February, August, May, and November (Figures 5–6) illustrate the seasonal cycle of global surface currents. For example, the eastward Wyrтки Jet in the equatorial Indian Ocean is prominent in May ($\sim 50 \text{ cm s}^{-1}$) and November ($\sim 70 \text{ cm s}^{-1}$) while being absent in August and reversed in February [e.g., Nagura and McPhaden, 2010]. Likewise the Somali Current is completely spun up in August during the Southwest Monsoon, but reversed in February near the end of the Northeast Monsoon [e.g., Schott *et al.*, 1990]. The Bay of Bengal shows a strong seasonal cycle as well, with current directions reversing completely [e.g., Shenoi *et al.*, 1999]. Interior flow across the equator is largely southward in August, and northward in February, with seasonally reversing surface winds driving a shallow “cross-equatorial roll” with subsurface flow opposite the surface flow [e.g., Schott *et al.*, 2002]. Further to the south, the surface expression of the South Equatorial Current is substantially weaker in August than in other seasons.

The seasonality of the NECC is clearly seen in the Pacific and Atlantic basins, revealing for example an intense Atlantic NECC emerging from the North Brazil Current Retroflection in August while neither exists in May [e.g., Lumpkin and Garzoli, 2005]. The Pacific NECC is quite strong in August and November, but much weaker in February and May [e.g., Johnson *et al.*, 2002]. The South Equatorial Countercurrent in the western Pacific Ocean at 11–8°S is clearly seen in February (and also in December, January and March, not shown) while being absent in other months [Chen and Qiu, 2004].

The gyre-scale surface circulations (Figures 5–6, streamlines) also exhibit seasonal migrations, which are no doubt associated with seasonal wind shifts [vis., Risien and Chelton, 2008]. For example, the centers of the northern hemisphere subtropical gyres shift to the south in February and to the north in August. In the North Pacific Ocean there is a dramatic shift in the latitude of the interior recirculation gyre, from ~20°N in February to ~40°N in August. This seasonal migration may have a significant modulating impact on the convergence of floating material in the “garbage patch” of the North Pacific, compared to calculations based on time-mean Lagrangian displacement statistics [e.g., Maximeko *et al.*, 2012] in which these shifts would spuriously increase the inferred time-mean lateral diffusivity.

3.4.1 Tropical west Pacific surface currents

Many fine-scale details of the surface circulation are difficult to see when plotted at the global scale, but are resolved by the drifter observations in the climatology presented here. For example, in the western Pacific (Figure 7) the southward-flowing

Mindanao Current can be seen to split immediately north of the northeastern tip of the Celebes year-round, with the westward branch entering the Celebes Sea, and the eastward branch feeding the NECC; the cyclonic Mindanao Eddy is located between the Mindanao Current and NECC throughout the year [c.f., *Arruda and Nof*, 2003]. In Boreal winter, the strongly zonal NECC separates into its main branch running along $\sim 5^{\circ}\text{N}$ and a secondary branch flowing ESE along the northwestern New Guinea coast (Figure 7). This branch reverses through Boreal spring, and by August the WNW New Guinea Coastal Current (NGCC) has surfaced. At the confluence of the Mindanao Current's eastward branch and the NGCC, a narrow northeastward-flowing jet develops, the eastern side of which recirculates to form the Halmahera Eddy [c.f., *Arruda and Nof*, 2003], which is not present in Boreal winter but is clearly visible in Boreal summer through fall. This eddy is thought to play a significant role in modulating exchange between the Pacific and Indian basins through the Indonesian Throughflow [*Qu et al.*, 1999].

3.4.2. Interior equatorial surface divergence

The seasonal divergences in the equatorial interiors of the three ocean basins (Figure 8) contrast strongly. Equatorial divergence in the Indian Ocean peaks in August with the relaxation of the Wyrtki Jet; the flow is strongly convergent in November through January. An off-equatorial divergence is evident in the South Indian Ocean, centered near 8°S in December–April, and closer to 5°S in May–August. This feature may be associated with the thermocline ridge near that latitude in the South Indian Ocean [e.g., *Hermes and Reason*, 2008]. In contrast, equatorial divergence is present year-round in the central Pacific and Atlantic basins [e.g., *Hansen and Paul*, 1987; *Johnson et al.*,

2001; Grodsky and Carton, 2002], although the magnitude displays a seasonal modulation in both basins with stronger divergence in Boreal spring vs. Boreal fall (mirroring the development of the cold tongue in the eastern regions of these basins). Off-equatorial convergence is seen throughout the year in the central Pacific south of the equator, but is more seasonally modulated to the north with a convergence maximum at 4–5°N in May–June. In the central Atlantic, convergent maxima are seen at 4–8° N during May–August, and at 6–4°S during June–September. These patterns of equatorial divergence and off-equatorial convergence are associated with the shallow tropical overturning cells in these basins [e.g., Perez *et al.*, 2010].

4. Summary and Discussion

We use a global set of drogued drifter velocity measurements to map the time-mean, seasonal, and SOI-related components of near-surface currents at high resolution. Our approach combines aspects of three previous mapping efforts [Bauer *et al.*, 1998; Johnson, 2001; Lumpkin, 2003] to address spatial and temporal variations in the data and to produce formal error bars for the various components (mean, seasonal cycle, and SOI regression) of the currents. Our analysis also takes advantage of data set corrections from a recent reevaluation of drogue presence [Lumpkin *et al.*, 2013], one result of which is significantly reduced speeds for currents such as the ACC. However, it is possible that downwind (and down-wave) slip, which has not been directly measured for drogued drifters at wind speeds $>10 \text{ m s}^{-1}$ [Niiler *et al.*, 1995], may exceed the linear slip removed in the recent data set update by Lumpkin *et al.* [2013], and as such there may still be downwind bias in regions of strong winds.

Assuming a mean density of 1025 kg m^{-3} , the global distribution of total kinetic energy (Figure 9d) amounts to a total of $4.6 \times 10^{17} \text{ J}$ in the upper 30 m, in all bins with more than 10 drifter days of data (for reference, the global total variable kinetic energy of the full-depth ocean is estimated at $3.8 \times 10^{18} \text{ J}$ [Wunsch, 1998]). Our estimate does not include energy at Lagrangian periods shorter than five days including inertial, tidal, submesoscale, and high-frequency mesoscale motions. Mean currents contribute a substantial fraction to the total kinetic energy (Figure 9a) where one would expect: in the western boundary currents and their extensions, in the North Equatorial currents and the North Equatorial countercurrents of the Atlantic and Pacific oceans, and in segments of the Antarctic Circumpolar Current. These are all locations where the total kinetic energy is high (Figure 9d), and – except for the equatorial currents and regions of the ACC – where there is topographic confinement. However, the mean currents also constitute a substantial fraction of the total kinetic energy in the South Equatorial currents of all three oceans as well as in the interior of the subpolar North Pacific gyre, all eddy desert regions (with the exception of the Indian Ocean SEC) where the total kinetic energy is relatively low. Globally, the mean currents contribute $1.6 \times 10^{17} \text{ J}$ of kinetic energy in the upper 30 m, 36% of the total estimated KE in bins with > 10 drifter days of observations.

The seasonal contribution (Figure 9c) to the total kinetic energy (Figure 9d) is 20–40% in the Pacific and Atlantic North Equatorial countercurrents. It is substantial throughout much of the Indian Ocean north of about 10°S , with maxima of 50–70% at 0 – 5°N , 55 – 70°E . Another location of strong seasonal contribution is the eastern tropical South Atlantic Ocean, just west of Africa: it contributes 20–30% of the total KE throughout the Angola Basin, and 40–70% against the African coast. Seasonal variations

represent a global total of 6.7×10^{16} J of kinetic energy in the upper 30 m in all bins with > 90 drifter days of observations, 15% of the total KE in those bins.

The fractional contribution of SOI-related variations (not shown) is generally small, exceeding 10% only in the vicinity of the equator from 165°E to 165°W. It represents a global total of 2.6×10^{15} J of kinetic energy in the upper 30 m in all bins with > 365 drifter days of observations, 1% of the total in those bins.

The eddy contribution (Figure 9b) to the total kinetic energy (Figure 10d) dominates much of the ocean, especially the interior of the subtropical gyres and the subpolar North Atlantic Gyre. The fraction of the total kinetic energy accounted for by eddies with Lagrangian periods > 5 days exceeds 50% in 69% of bins with > 10 drifter days of observations. However, in much of this area the total kinetic energy is small.

EKE dominates in the well-known eddy regions such as the Gulf Stream and Kuroshio recirculation gyres, Agulhas and North Brazil Current ring pathways, and the

Brazil/Malvinas Confluence. Eddies also make a large contribution between the North Equatorial currents and the various branches of the South Equatorial currents, where tropical instability waves [e.g., *Chelton et al.*, 1999] are energetic. The eddy deserts of

the eastern North Pacific, eastern South Atlantic, and eastern South Pacific each have portions where mean currents are dominant, but also portions where the eddies are

dominant, with low total energy levels throughout. The EKE represents a total of 2.4×10^{17} J of kinetic energy in the upper 30 m in all bins with > 10 drifter days of

observations, 49% of the total KE in those bins. As noted above, eddy energy at periods shorter than five days is not included in this value. These higher frequencies include the

peak in Lagrangian spectra at or near the inertial period; examination of this wind energy input can be found elsewhere [e.g., *Elipot et al.*, 2010].

The time-mean and seasonal currents derived here can be used for purposes such as model validation and product evaluation. For example, there are large and spatially coherent differences (Figure 10a) between the mean velocity in the drifter climatology and the January 1993–December 2003 mean velocity from the $1/3^\circ$ unfiltered satellite-derived Ocean Surface Current Analysis Real-time (OSCAR) product [*Bonjean and Lagerloef*, 2002] including geostrophic, Ekman, and buoyancy components. While inter-annual variations may play a role in some of the discrepancies, the drifter climatology is faster by up to $20\text{--}25\text{ cm s}^{-1}$ in the Gulf Stream and Kuroshio currents, and up to 35 cm s^{-1} faster in segments of the ACC and Agulhas Return Current. Along the northern branch of the South Equatorial Current at $1\text{--}3^\circ\text{N}$ in the Pacific, the drifter climatology is $20\text{--}50\text{ cm s}^{-1}$ faster to the west than in the OSCAR product; on the equator in the Atlantic it is $20\text{--}35\text{ cm s}^{-1}$ faster to the west (Figure 10). These dramatic differences may be due both to smoothing and neglect of higher order dynamics such as near-equatorial current shear and stratification [*Jacob Wenegrat*, manuscript in preparation, 2013] in OSCAR. Surface currents from OSCAR are available at 5-day resolution, similar to the 5-day half-power cut-off of the filter applied here to the drifter data, so different sampling time is unlikely to be the primary cause of the observed differences.

Differences between this new drifter-derived climatology and products giving time-mean geostrophic speed (such as the CNES-CLS09 MDT product [*Rio et al.* 2011], Figure 10b) can be used to infer the ageostrophic component of drifter motion. Although it extends beyond the scope of this study, it would be interesting to remove the

ageostrophic motion, recalculate the distribution of variance about the time-mean speeds, and compare the results to eddy kinetic energy from altimetry [c.f., *Fratantoni*, 2001].

Because the drifter climatology gives total near-surface currents, it can also be used to improve our estimates of wind stress and turbulent heat fluxes, which depend on the relative speed of the wind over the moving ocean surface [*Fairall et al.*, 2003]. Ocean currents have been demonstrated to affect the wind stress field and its curl and divergence [*Kelly et al.*, 2001; *Risien and Chelton*, 2008].

Our results include formal error bars for all coefficients in the model (1). These error bars (Figure 11) demonstrate where currents are well-resolved by the data, and conversely where more data are needed. Absolute error estimates (Figure 11, left panels) are generally large where the signals are large (Figures 2, 4) and where observations are sparse (Figure 1). The signal-to-noise ratio for the time-mean current speed (Figure 11b) is small in areas with weak time-mean currents such as the centers of the subtropical gyres. Elsewhere, this ratio indicates that time-mean currents are well-resolved away from seasonally ice-covered regions except in four areas: (1) the ACC in the central and eastern South Pacific; (2) the southwestern and northwestern Gulf of Mexico, west of 90°W excluding the well-resolved Loop Current pathway; (3) the Indonesian Sea, which is relatively shallow and undersampled by drifters (Figure 1); and (4) the Coral Sea. Seasonal variations are well-resolved throughout the tropical Pacific, along the path of the NECC in the central and western tropical Atlantic, and off the equator in the tropical Indian basins. Seasonal variations are more marginally resolved in the Gulf of Guinea and southern tropical Atlantic and equatorial Indian oceans (Figure 11d), where observations are more sparse (Figure 1). Time-mean and seasonal error estimates are

large in regions of seasonal or near-permanent ice coverage. The SOI-related coefficient is well-resolved in the central and western tropical Pacific and across the central and eastern tropical Indian basins, but (as noted earlier) is not well resolved by the data on the equator east of 145°W owing to sparse observational density.

The climatology of time-mean and seasonal currents derived in this study, along with the model coefficients and associated errors, is available at http://www.aoml.noaa.gov/phod/dac/dac_meanvel.php. Animations of these currents in various regions are available at http://www.aoml.noaa.gov/phod/dac/dac_animations.php.

Acknowledgments. NOAA Research and the NOAA Climate Program Office funded this work. RL received additional support from the Atlantic Oceanographic and Meteorological Laboratory and GCJ from the Pacific Marine Environmental Laboratory. Conversations and input from Chris Meinen, Carlisle Thacker, Kathleen Dohan, Semyon Grodsky, Jacob Weneprat, Frank Bryan, and three anonymous reviewers helped improve the original manuscript. The drifter data were collected and made freely available by the Global Drifter Program (<http://www.aoml.noaa.gov/envids/gld/index.php>). OSCAR data are available at <http://www.oscar.noaa.gov>. PMEL publication 3902.

References

- Arruda, W. Z. and D. Nof (2003), The Mindanao and Halmahera Eddies–Twin Eddies Induced by Nonlinearities, *J. Phys. Oceanogr.*, *33*, 2815–2830.
- Baker, D. J. (1982), A note on Sverdrup balance in the Southern Ocean, *J. Mar. Res.*, *40*, (Suppl.), S21–S26.
- Bauer, S., M. S. Swenson, A. Griffa, A. J. Mariano, and K. Owens (1998), Eddy–mean flow decomposition and eddy-diffusivity estimates in the tropical Pacific Ocean. 1. Methodology, *J. Geophys. Res.*, *103*(C13), 30,855–30,871, doi:10.1029/1998JC900009.
- Bograd, S. J., I. Schroeder, N. Sarkar, X. Qiu, W. J. Sydeman, and F. B. Schwing (2009), Phenology of coastal upwelling in the California Current, *Geophys. Res. Lett.*, *36*, L01602, doi:10.1029/2008GL035933.
- Bonjean, F. and G. S. Lagerloef (2002). Diagnostic Model and Analysis of the Surface Currents in the Tropical Pacific Ocean, *J. Phys. Oceanogr.*, *32*, 2938–2954.
- Cai, W., and co-authors (2012), More extreme swings of the South Pacific convergence zone due to greenhouse warming, *Nature*, *488*, 365–369, doi:10.1038/nature11358.
- Chelton, D. B., R. A. deSzoeki, M. G. Schlax, K. El Naggar, and N. Siwertz (1998), Geographical variability of the first baroclinic Rossby radius of deformation, *J. Phys. Oceanogr.*, *28*, 433–460. doi: [http://dx.doi.org/10.1175/1520-0485\(1998\)028<0433:GVOTFB>2.0.CO;2](http://dx.doi.org/10.1175/1520-0485(1998)028<0433:GVOTFB>2.0.CO;2).
- Chelton, D. B., F. J. Wentz, C. L. Gentemann, R. A. de Szoeki, and M. G. Schlax (2000), Satellite microwave SST observations of transequatorial tropical instability waves, *Geophys. Res. Lett.*, *27*, 1239–1242, doi:10.1029/1999GL011047.

Chen, S., and B. Qiu (2004), Seasonal variability of the South Equatorial Countercurrent, *J. Geophys. Res.*, *109*, C08003, doi:10.1029/2003JC002243.

Colas, F., J. C. McWilliams, X. Capet and J. Kurian (2012), Heat balance and eddies in the Peru-Chile current system, *Climate Dynamics*, *39*, 509–529, doi: 10.1007/s00382-011-1170-6.

Davidson, F. J. M., A. Allen, G. B. Brassington, Ø. Breivik, P. Daniel, M. Kamachi, S. Sato, B. King, F. Lefevre, M. Sutton, and H. Kaneko (2009), Applications of GODAE ocean current forecasts to search and rescue and ship routing, *Oceanogr.* *22*(3):176–181, <http://dx.doi.org/10.5670/oceanog.2009.76>.

Ducet, N., P.-Y. Le Traon, and G. Reverdin (2000), Global high-resolution mapping of ocean circulation from TOPEX/Poseidon and ERS-1 and -2, *J. Geophys. Res.*, *105*, 19,477–19,498, doi:10.1029/2000JC900063.

Elipot, S., R. Lumpkin, and G. Prieto (2010), Modification of inertial oscillations by the mesoscale eddy field. *J. Geophys. Res.-Oceans*, *115*, C09010, doi:10.1029/2009JC005679.

Fairall, C.W., Bradley, E.F., Hare, J.E., Grachev, A.A., and Edson, J.B. (2003), Bulk parameterization of air-sea fluxes: Updates and verification for the COARE algorithm, *J. Climate*, *16*, 571–591.

Falco, P., and E. Zambianchi (2011), Near-surface structure of the Antarctic Circumpolar Current derived from World Ocean Circulation Experiment drifter data, *J. Geophys. Res.*, *116*, C05003, doi:10.1029/2010JC006349.

Feng, M., G. Meyers, A. Pearce, and S. Wijffels (2003), Annual and interannual variations of the Leeuwin Current at 32°S, *J. Geophys. Res.*, *108*, 3355,

doi:10.1029/2002JC001763.

Fiedler, P. C. (2002), The annual cycle and biological effects of the Costa Rica Dome.

Deep-Sea Res. II, 49, 321–338, doi: 10.1016/S0967-0637(01)00057-7.

Fratantoni, D. M. (2001), North Atlantic surface circulation during the 1990's observed with satellite-tracked drifters, *J. Geophys. Res.-Oceans*, 106 (C10), 22,067–22,093.

Ganachaud, A., L. Gourdeau, and W. Kessler (2008), Bifurcation of the subtropical South Equatorial Current against New Caledonia in December 2004 from a hydrographic inverse box model, *J. Phys. Oceanogr.*, 38, 2072–2084, doi:10.1175/2008JPO3901.1.

Garzoli, S. L., A. Field, W. E. Johns, and Q. Yao (2004), North Brazil Current retroflection and transports, *J. Geophys. Res.*, 109, C01013,

doi:10.1029/2003JC001775.

Gordon, A. L., S. Ma, D. B. Olson, P. Hacker, A. Field, L. D. Talley, D. Wilson, and M. Baringer (1997), Advection and diffusion of Indonesian Throughflow Water within the Indian Ocean South Equatorial Current, *Geophys. Res. Lett.*, 24, 2573–2576, doi:10.1029/97GL01061.

Griffa, A., R. Lumpkin, and M. Veneziani (2008), Cyclonic and anticyclonic motion in the upper ocean, *Geophys. Res. Lett.*, 35, L01608, doi:10.1029/2007GL032100.

Grodsky, S. A. and J. A. Carton (2002), Surface drifter pathways originating in the equatorial Atlantic cold tongue, *Geophys. Res. Lett.*, 29, 2147,

doi:10.1029/2002GL015788.

Grodsky, S. A., R. Lumpkin, and J. A. Carton (2011), Spurious trends in global surface drifter currents, *Geophys. Res. Lett.*, 38, L10606, doi:10.1029/2011GL047393.

Hansen, D. V., and C. A. Paul (1987), Vertical motion in the eastern equatorial Pacific

inferred from drifting buoys. *Oceanol. Acta*, 6, 27–32.

Hansen, D., and P.-M. Poulain (1996), Quality control and interpolations of WOCE-

TOGA drifter data, *J. Atmos. Oceanic Technol.*, 13, 900–909.

Hermes, J. C., and C. J. C. Reason (2008), Annual cycle of the South Indian Ocean

(Seychelles-Chagos) thermocline ridge in a regional ocean model, *J. Geophys. Res.*, 113, C04035, doi:10.1029/2007JC004363.

Higginson, S., K. R. Thompson, J. Huang, M. Véronneau, and D. G. Wright (2011), The

mean surface circulation of the North Atlantic subpolar gyre: A comparison of estimates derived from new gravity and oceanographic measurements, *J. Geophys. Res.*, 116, C08016, doi:10.1029/2010JC006877.

Hurrell, J.W. (1995), Decadal trends in the North Atlantic Oscillation: Regional

temperatures and precipitation, *Science*, 269, 676–679.

Hutchings, L., and co-authors (2009), The Benguela Current: An ecosystem of four

components, *Prog. Oceanogr.*, 83, 15–32, doi:10.1016/j.pocean.2009.07.046.

Jakobsen, P. K., M. H. Ribergaard, D. Quadfasel, T. Schmith, and C. W. Hughes (2003),

Near-surface circulation in the northern North Atlantic as inferred from Lagrangian drifters: Variability from the mesoscale to interannual, *J. Geophys. Res.*, 108(C8), 3251, doi:10.1029/2002JC001554.

Johnson, G. C. (2001), The Pacific Ocean subtropical cell surface limb. *Geophys. Res.*

Lett., 28, 1771–1774, doi:10.1029/2000GL012723.

Johnson, G. C., M. J. McPhaden, and E. Firing (2001), Equatorial Pacific Ocean

horizontal velocity, divergence, and upwelling. *J. Phys. Oceanogr.*, 31, 839–849, doi:10.1175/1520-0485(2001)031<0839:EPOHVD>2.0.CO;2.

- Johnson, G. C., M. J. McPhaden, G. D. Rowe, and K. E. McTaggart (2000). Upper equatorial Pacific Ocean current and salinity variability during the 1996–1998 El Niño–La Niña cycle. *J. Geophys. Res.*, *105*, 1037–1053, doi:10.1029/1999JC900280.
- Johnson, G. C., B. M. Sloyan, W. S. Kessler, and K. E. McTaggart (2002), Direct measurements of upper ocean currents and water properties across the tropical Pacific Ocean during the 1990's, *Progress in Oceanography*, *52*, 31–61, doi:10.1016/S0079-6611(02)00021-6.
- Kelly, K. A., S. Dickinson, M. J. McPhaden, and G. C. Johnson (2001), Ocean currents evident in satellite wind data, *Geophysical Research Letters*, *28*, 2469–2472, doi:10.1029/2000GL012610.
- Klein, B., and G. Siedler (1989), On the origin of the Azores Current, *J. Geophys. Res.*, *94*, 6159–6168, doi:10.1029/JC094iC05p06159.
- Koszalka, I, J. H. LaCasce, M. Andersson, K. A. Orvikb, and C. Mauritzen (2011), Surface circulation in the Nordic Seas from clustered drifters, *Deep-Sea Res. I*, *58*, 468–485, doi:10.1016/j.dsr.2011.01.007.
- Law, K. L., S. Morét-Ferguson, N. A. Maximenko, G. Proskurowski, E. E. Peacock, J. Hafner, and C. M. Reddy (2010), Plastic Accumulation in the North Atlantic Subtropical Gyre, *Science*, *329*, 1185–1188, doi:10.1126/science.1192321.
- Lumpkin, R. (2003), Decomposition of surface drifter observations in the Atlantic Ocean, *Geophys. Res. Lett.*, *30* (14), 1753, doi:10.1029/2003GL017519.
- Lumpkin, R. and S. Garzoli (2005), Near-surface circulation in the Tropical Atlantic Ocean, *Deep-Sea Res. I*, *52*, 495–518.
- Lumpkin, R., and M. Pazos (2007), Measuring surface currents with Surface Velocity

Program drifters: the instrument, its data and some recent results, in Lagrangian Analysis and Prediction of Coastal and Ocean Dynamics, edited by A. Griffa, A. D. Kirwan, A. Mariano, T. Özgökmen, and T. Rossby, chap. 2, pp. 39–67, Cambridge University Press.

Lumpkin, R. and S. L. Garzoli (2011), Interannual to Decadal Variability in the Southwestern Atlantic's Surface Circulation, *J. Geophys. Res.-Oceans*, 116, C01014, doi:10.1029/2010JC006285.

Lumpkin, R., S. Grodsky, L. Centurioni, M.-H. Rio, J. Carton and D. Lee (2012), Removing spurious low-frequency variability in drifter velocities, *J. Atmos. Oceanic Technol.*, in revision [minor revisions necessary].

Lutjeharms, J. R. E. (2007). Three decades of research on the greater Agulhas Current, *Ocean Sci.*, 3, 129–147, doi:10.5194/os-3-129-2007.

Mantua, N.J. and S.R. Hare, Y. Zhang, J.M. Wallace, and R.C. Francis (1997), A Pacific interdecadal climate oscillation with impacts on salmon production, *Bull. Am. Meteorol. Soc.*, 78, 1069–1079.

Mason, E., F. Colas, and J. Pelegrí (2012), A Lagrangian study tracing water parcel origins in the Canary Upwelling System, *Scientia Marina*, 76(S1), 79–94, doi:10.3989/scimar.03608.18D.

Maximenko, N., P. Niiler, M.-H. Rio, O. Melnichenko, L. Centurioni, D. Chambers, V. Zlotnicki, and B. Galperin (2009), Mean dynamic topography of the ocean derived from satellite and drifting buoy data using three different techniques, *J. Atmos. Oceanic Technol.*, 26, 1910–1919, doi:10.1175/2009JTECHO672.1

Maximenko, N., J. Hafner, and P. Niiler (2012), Pathways of marine debris derived from

trajectories of Lagrangian drifters, *Mar. Pollut. Bull.*, 65, 51–62,

doi:10.1016/j.marpolbul.2011.04.016.

McCord, M. R., Y. K. Lee, and H. K. Lo (1999), Ship routing through altimetry-derived ocean currents, *Transport. Sci.*, 33, 49–67, doi:10.1287/trsc.33.1.49.

Molinari, R. L., and J. Morrison (1988), The separation of the Yucatan Current from the Campeche Bank and the intrusion of the Loop Current into the Gulf of Mexico, *J. Geophys. Res.*, 93, 10,645–10,654, doi:10.1029/JC093iC09p10645.

Nagura, M., and M. J. McPhaden (2010), Wyrтки Jet dynamics: Seasonal variability, *J. Geophys. Res.*, 115, C07009, doi:10.1029/2009JC005922.

Niiler, P. P. (2001), The world ocean surface circulation, in *Ocean Circulation and Climate*, International Geophysics Series, 77, edited by G. Siedler, J. Church, and J. Gould, pp. 193–204, Academic Press.

Niiler, P. P., A. Sybrandy, K. Bi, P. Poulain, and D. Bitterman (1995), Measurements of the water-following capability of holey-sock and TRISTAR drifters, *Deep Sea Res.*, 42, 1951–1964.

Niiler, P. P. and J. D. Paduan (1995), Wind-driven motions in the northeast Pacific as measured by Lagrangian drifters, *J. Phys. Oceanogr.* 25, 2819–2830.

Nyckjær, L., and L. Van Camp (1994), Seasonal and interannual variability of coastal upwelling along northwest Africa and Portugal from 1981 to 1991, *J. Geophys. Res.*, 99, 14,197–14,207, doi:10.1029/94JC00814.

Orsi, A. H., T. Whitworth III and W. D. Nowlin, Jr., (1995), On the meridional extent and fronts of the Antarctic Circumpolar Current, *Deep-Sea Res. I*, 42, 641–673.

Palacios, D. M. and S. J. Bograd (2005), A census of Tehuantepec and Papagayo eddies

in the northeastern tropical Pacific, *Geophys. Res. Lett.*, 32, 23606, doi:
10.1029/2005GL024324.

Pazan, S. E., and P. P. Niiler (2001), Recovery of near-surface velocity from undrogued drifters, *J. Atmos. Oceanic Technol.*, 18, 476–489.

Perez, R. C., M. F. Cronin and W. S. Kessler (2010), Tropical Cells and a Secondary Circulation near the Northern Front of the Equatorial Pacific Cold Tongue, *J. Phys. Oceanogr.*, 40, 2091–2106.

Potemra, J. T., and N. Schneider (2007), Interannual variations of the Indonesian throughflow, *J. Geophys. Res.*, 112, C05035, doi:10.1029/2006JC003808.

Poulain, P.-M., R. Gerin, E. Mauri, and R. Pennel (2009), Wind effects on drogued and undrogued drifters in the eastern Mediterranean, *J. Atmos. Oceanic Technol.*, 26, 1144–1156, doi:10.1175/2008JTECHO618.1.

Provost, C., O. Garcia, and V. Garçon (1992), Analysis of satellite sea surface temperature time series in the Brazil-Malvinas Current confluence region: Dominance of the annual and semiannual periods, *J. Geophys. Res.*, 97, 17,841–17,858, doi:10.1029/92JC01693.

Qu, T., H. Mitsudera, and B. Qiu (2001), A climatological view of the Kuroshio/Oyashio system east of Japan, *J. Phys. Oceanogr.*, 31, 2575–2589, doi:10.1175/1520-0485(2001)031<2575:ACVOTK>2.0.CO;2.

Qu, T., H. Mitsudera, and T. Yamagata (1999), A Climatology of the Circulation and Water Mass Distribution near the Philippine Coast, *J. Phys. Oceanogr.*, 29, 1488–1505.

Reed, R.K. (1984), Flow of the Alaskan Stream and its variations, *Deep-Sea Res.*, 31,

369–386, doi:10.1016/0198-0149(84)90090-6.

Richardson, P. L., and D. Walsh (1986), Mapping climatological seasonal variations of surface currents in the tropical Atlantic using ship drifts, *J. Geophys. Res.*, *91*, 10,537–10,550, doi:10.1029/JC091iC09p10537.

Richardson, P. L. (2005), Caribbean Current and eddies as observed by surface drifters, *Deep-Sea Res.*, *52*, 429–463, doi:10.1016/j.dsr2.2004.11.001.

Ridgway K.R., J.R. Dunn, and J.L. Wilkin (2002), Ocean interpolation by four-dimensional least squares - Application to the waters around Australia, *J. Atmos. Oceanic Technol.*, *19*, 1357–1375.

Rio, M. H., S. Guinehut, and G. Larnicol (2011), New CNES-CLS09 global mean dynamic topography computed from the combination of GRACE data, altimetry and in situ measurements, *J. Geophys. Res.*, *116*, C07,018, doi:10.1029/2010JCOO6505.

Risien, C. M., and D. B. Chelton (2008), A global climatology of surface wind and wind stress fields from eight years of QuikSCAT scatterometer data, *J. Phys. Oceanogr.*, *38*, 2379–2413, doi: 10.1175/2008JPO3881.1.

Rodrigues, R. R., L. M. Rothstein, and M. Wimbush (2007), Seasonal variability of the South Equatorial Current bifurcation in the Atlantic Ocean: A numerical study, *J. Phys. Oceanogr.*, *37*, 16–30.

Schmitz, W. J., Jr., and M. S. McCartney (1993), On the North Atlantic Circulation, *Rev. Geophys.*, *31*, 29–49, doi:10.1029/92RG02583.

Schott, F. A., and J. P. McCreary, Jr. (2001), The monsoon circulation of the Indian Ocean, *Prog. Oceanogr.*, *51*, 1–123.

Schott, F. A., J. P. McCreary, Jr., and G. C. Johnson (2004), Shallow overturning

circulations of the tropical-subtropical oceans, in *Earth Climate: The Ocean-Atmosphere Interaction*, C. Wang, S.-P. Xie, and J. A. Carton, Eds., American Geophysical Union Geophysical Monograph 147, 261–304.

Schott, F., J. C. Swallow, and M. Fieux (1990), The Somali current at the equator: annual cycle of currents and transports in the upper 1000 m and connection to neighbouring latitudes, *Deep-Sea Res. A*, *37*, 1825–1848, doi:10.1016/0198-0149(90)90080-F.

Sloyan, B. M., and S. R. Rintoul (2001). The Southern Ocean limb of the global deep overturning circulation, *J. Phys. Oceanogr.*, *31*, 143–173, doi:10.1175/1520-0485(2001)031<0143:TSOLOT>2.0.CO;2.

Stammer, D. (1997), Global characteristics of ocean variability estimated from regional TOPEX/POSEIDON altimeter measurements, *J. Phys. Oceanogr.*, *27*, 1743–1769. doi:10.1175/1520-0485(1997)027<1743:GCOOVE>2.0.CO;2

Swallow, J., M. Fieux, and F. Schott (1988), The Boundary Currents East and North of Madagascar 1. Geostrophic Currents and Transports, *J. Geophys. Res.*, *93*, 4951–4962, doi:10.1029/JC093iC05p04951.

Thompson, D. W. J., and J. M. Wallace (2000), Annular modes in the extratropical circulation. Part I: Month-to-month variability, *J. Climate*, *13*, 1000–1016.

Toole, J. M., R. C. Millard, Z. Wang, and S. Pu (1990), Observations of the Pacific North Equatorial Current bifurcation at the Philippine coast, *J. Phys. Oceanogr.*, *20*, 307–318, doi:10.1175/1520-0485(1990)020<0307:OOTPNE>2.0.CO;2.

Trenberth, K. E. (1984), Signal versus noise in the Southern Oscillation, *Mon. Weath. Rev.*, *112*, 326–332.

Accepted Article
van Sebille, E., M. H. England and G. Froyland (2012), Origin, dynamics and evolution of ocean garbage patches from observed surface drifters, *Environ. Res. Lett.* 7,

044040, doi:10.1088/1748-9326/7/4/044040.

Wunsch, C. (1996), *The Ocean Circulation Inverse Problem*, Cambridge University Press, New York.

Wunsch, C. (1998), The Work Done by the Wind on the Oceanic General Circulation, *J. Phys. Oceanogr.*, 28, 2332–2340.

Yoder, J. A., S. G. Ackleson, R. T. Barber, P. Flament, and W. M. Balch (1994), A line in the sea, *Nature*, 371, 689–692, doi:10.1038/371689a0.

Figure Captions

Figure 1. Number of drogued drifter observations used to map fields at each grid point bin (in drifter days per square degree). Thresholds for estimating a mean field (0.8 drifter days per square degree, red lines), a seasonal cycle (7 days per square degree, orange lines), and a SOI regression (29 days per square degree, black lines) are contoured.

Figure 2. Mean current speeds (colors, in cm s^{-1}) from near-surface surface drifter data with streamlines (black lines). Streamlines are calculated from spatially smoothed currents to indicate flow direction and qualitatively illustrate large-scale circulation features, including surface divergence. Light gray areas have less than 10 drifter days per bin (0.8 per square degree). In addition, only bins with mean current speeds statistically different from zero at one standard error of the mean are shaded. Inset (top left) shows histogram of mean current speed (cm s^{-1} , horizontal axis, from 0 to 100 at 3.125 cm s^{-1} intervals) vs. number of bins (in kilobins, vertical axis, from 0 to 25,000 bins).

Figure 3. Variance ellipses centered every 5° longitude by 2° latitude (black lines) over the square root of the magnitude of variance (colors in cm s^{-1}). Light gray areas have less than 0.8 drifter days per square degree.

Figure 4. Velocity of currents regressed onto the Southern Oscillation Index (colors in cm s^{-1}) shown for $\text{SOI} = -1$ (moderate El Niño) with directions (black arrows) indicated at for a subset of gridpoints. Arrows not shown where their magnitude is not significantly

different from zero. Light gray areas have less than 365 drifter days per bin (29 per square degree).

Figure 5. Near-surface ocean currents from surface drifter data. Details follow Figure 2, except displayed for climatological February (top panel) and August (bottom panel).

Light gray areas have less than 90 drifter days per bin (7 per square degree).

Figure 6. Near-surface ocean currents from surface drifter data. Details follow Figure 2, except displayed for climatological May (top panel) and November (bottom panel).

Light gray areas have less than 90 drifter days per bin (7 per square degree).

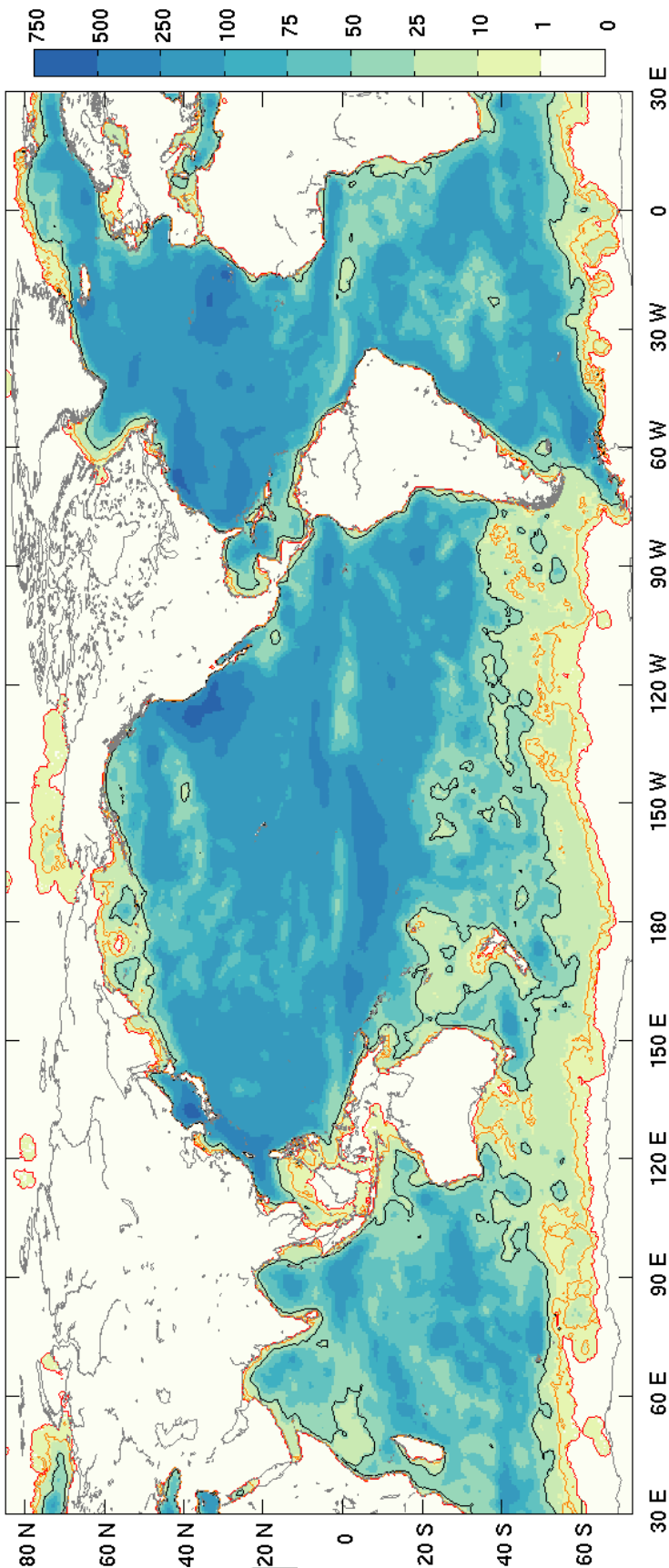
Figure 7. Seasonal variations of surface currents (black arrows, see key in lower left panel) in the northwestern tropical Pacific Ocean. Currents are not shown where they are not significantly different from zero at one standard error of the mean.

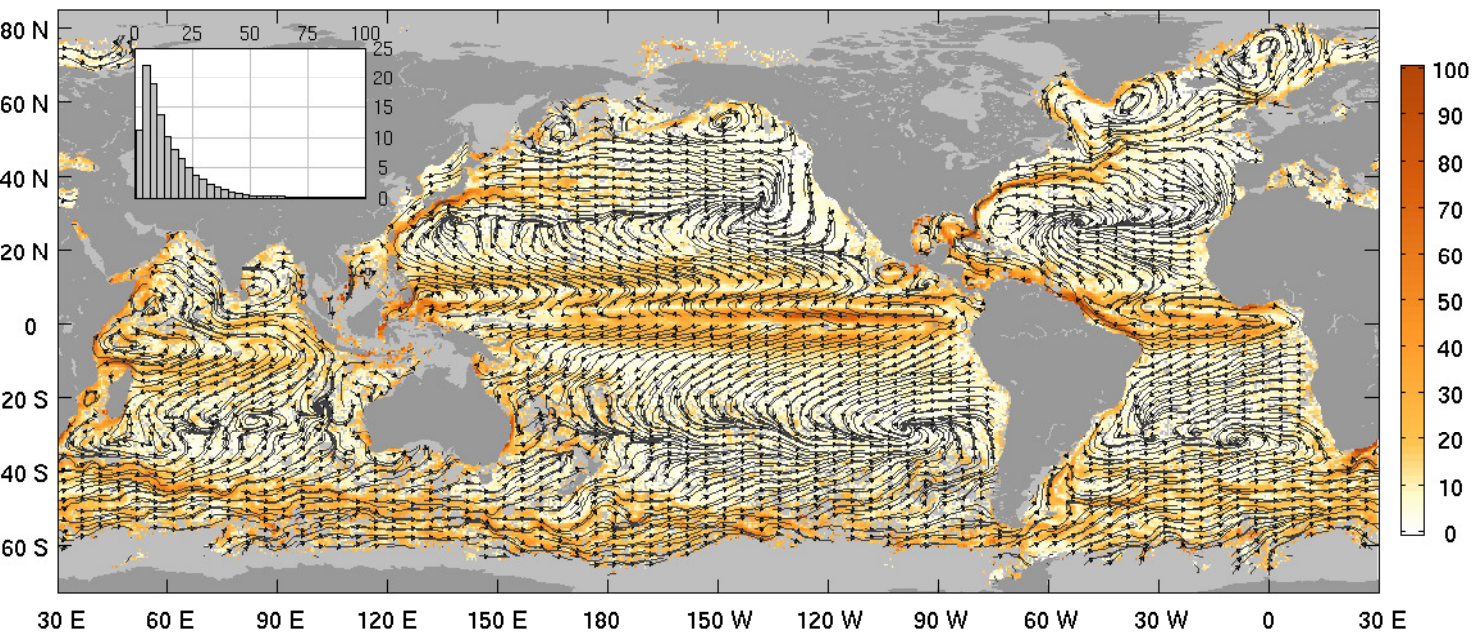
Figure 8. Seasonal cycle of surface divergence (colors, 10^{-8} s^{-1}) vs. latitude averaged over longitude bands in the interior of the a) Indian ($90^{\circ}\text{E} - 55^{\circ}\text{E}$), b) Pacific ($165^{\circ}\text{E} - 85^{\circ}\text{W}$), and c) Atlantic ($30^{\circ}\text{W} - 5^{\circ}\text{E}$) Oceans. Tick marks show the start of named months.

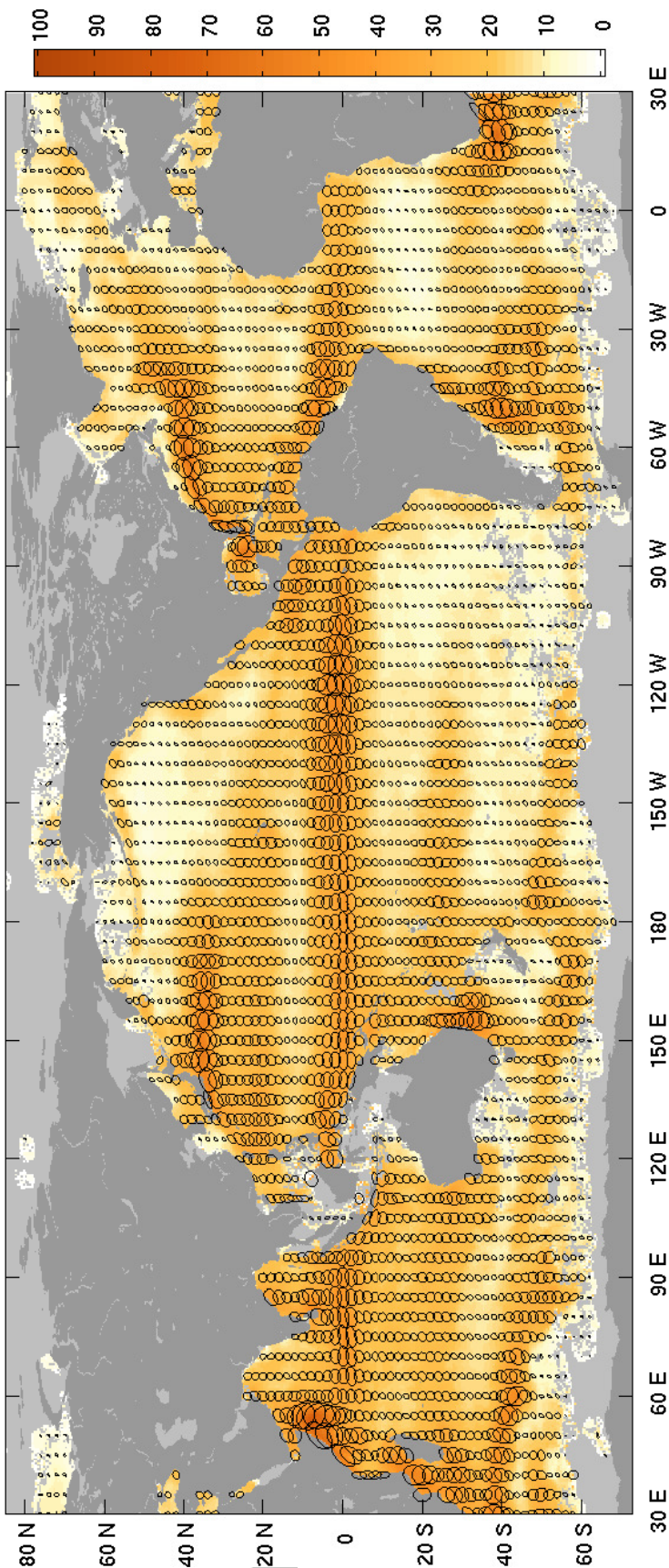
Figure 9. Fractions (colors, upper colorbar) of (a) time-mean, (b), eddy, and (c) seasonal contributions to the total surface kinetic energy in the drifter climatology along with (d) the total kinetic energy (colors, $\text{m}^2 \text{ s}^{-2}$, lower colorbar).

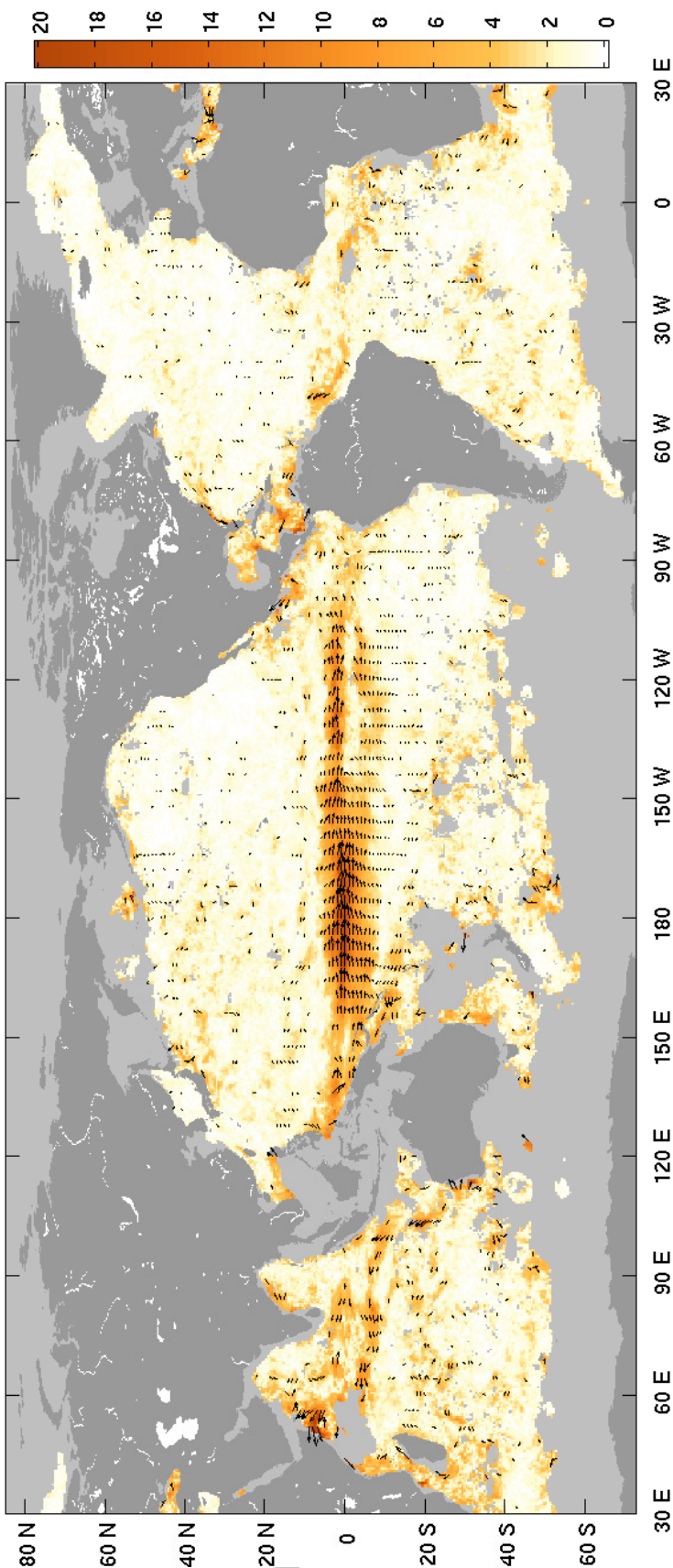
Figure 10. Vector differences (arrows; colors indicate difference magnitudes in cm s^{-1}), of a) time-mean velocity of drifters minus January 1993–December 2003 time-mean total speed from NOAA’s 1/3 degree unsmoothed Ocean Surface Current Analysis Real-time (OSCAR) product [Bonjean and Lagerloef, 2002] including geostrophic, Ekman and buoyancy components, and b) time-mean velocity of drifters minus time-mean geostrophic velocity from the CNES-CLS 2009 v1.1 Mean Dynamic Topography [Rio *et al.*, 2011].

Figure 11: Left column: absolute error (square root of the sum of the squared errors) in (a) time-mean speed, (c) speed of seasonal variations (annual and semiannual) and (e) SOI-correlated currents (cm s^{-1} ; color bar adjacent to e). Right column: signal-to-noise ratio, i.e., magnitude of the coefficient (or square root of the sum of the squared coefficients) divided by the error estimates, for (b) absolute speed, (d) speed of seasonal variations, and (f) SOI-correlated currents (color bar adjacent to f).

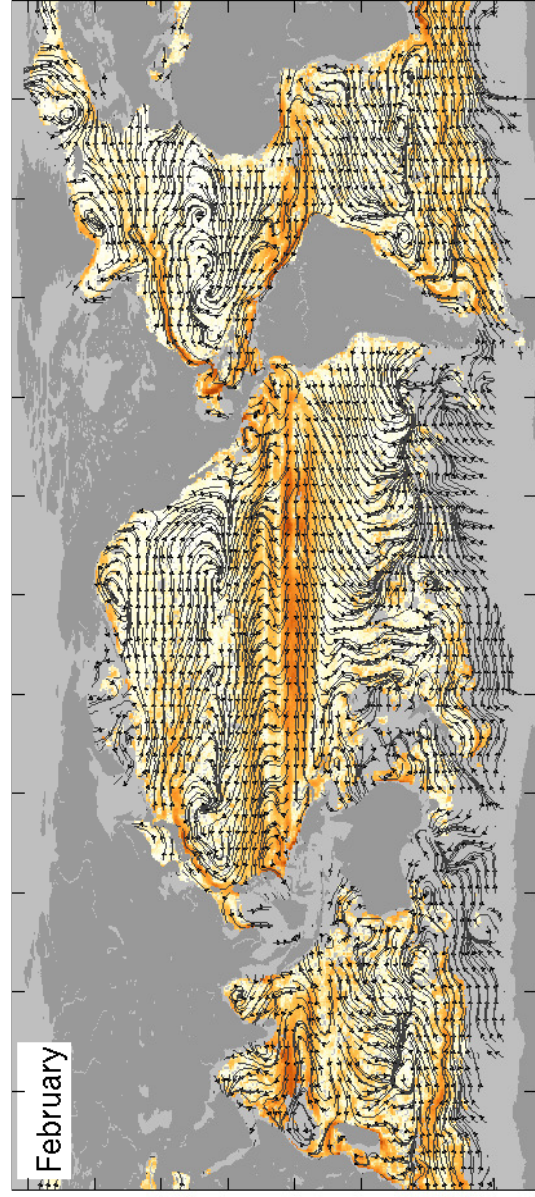




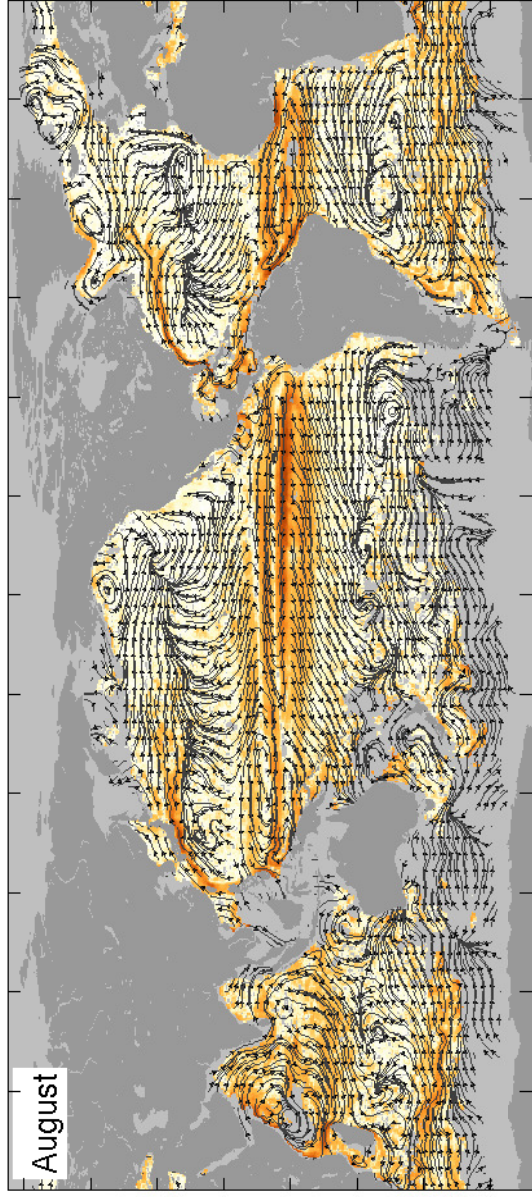


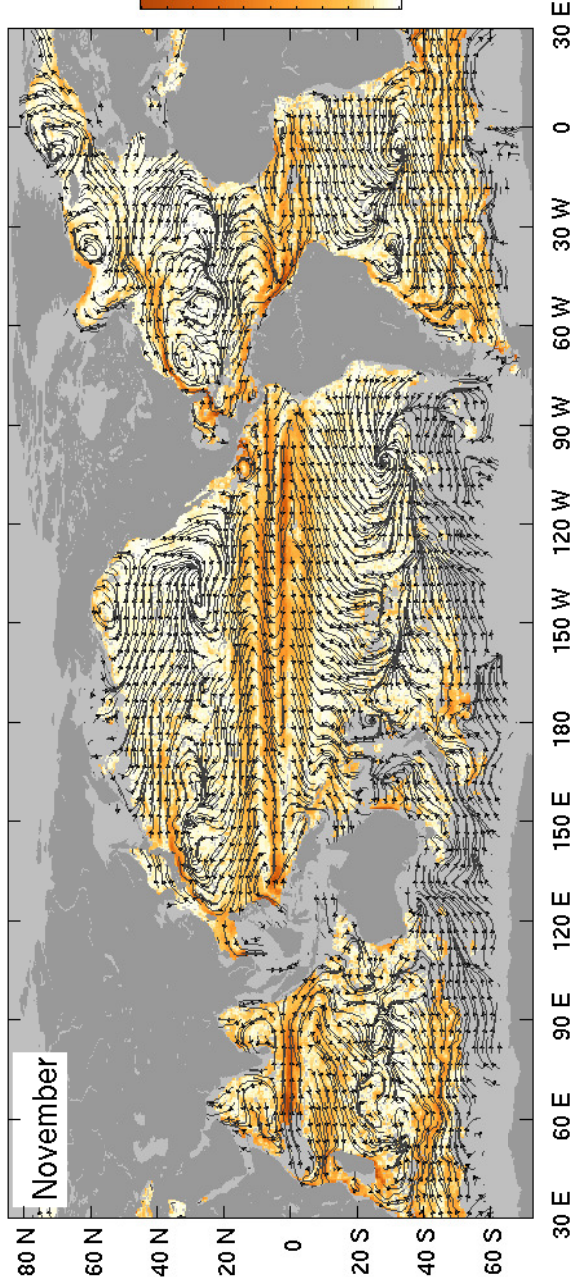
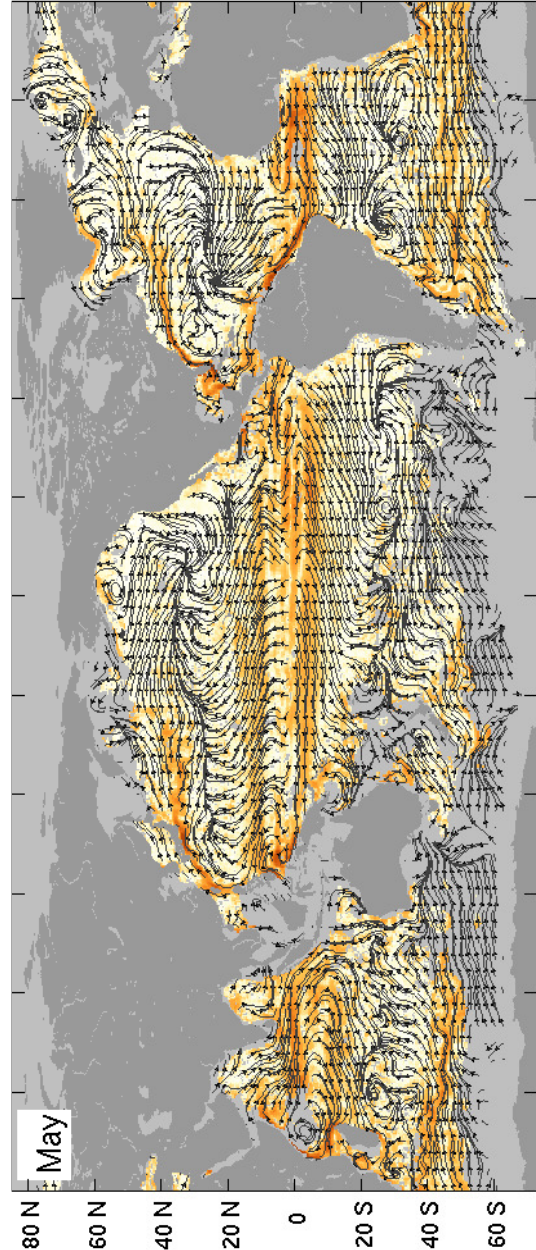


February

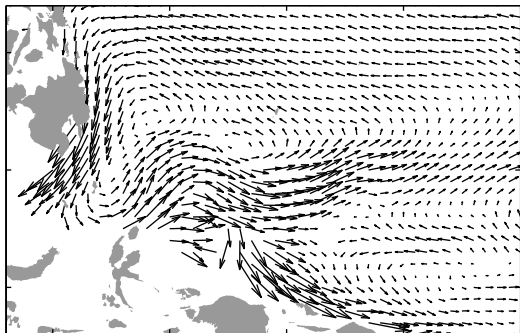


August

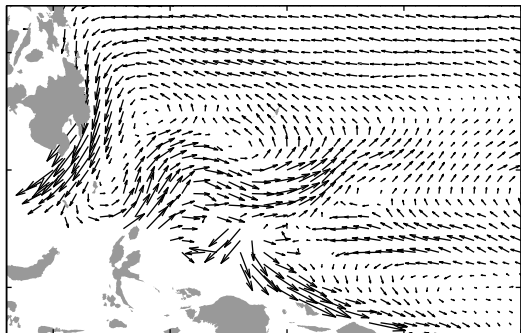




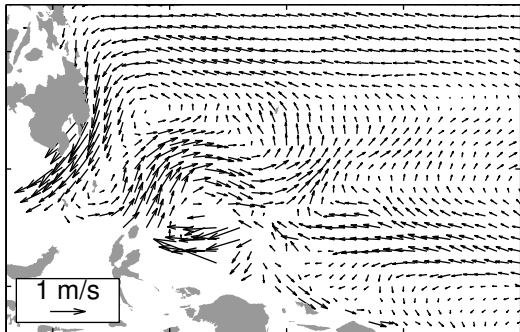
February



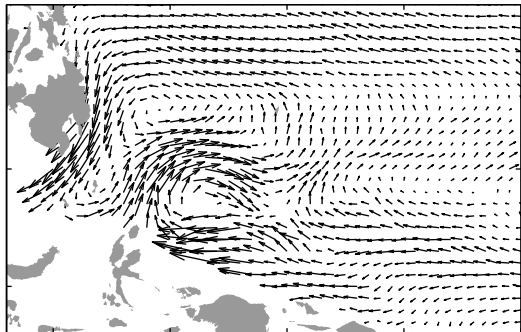
May



August

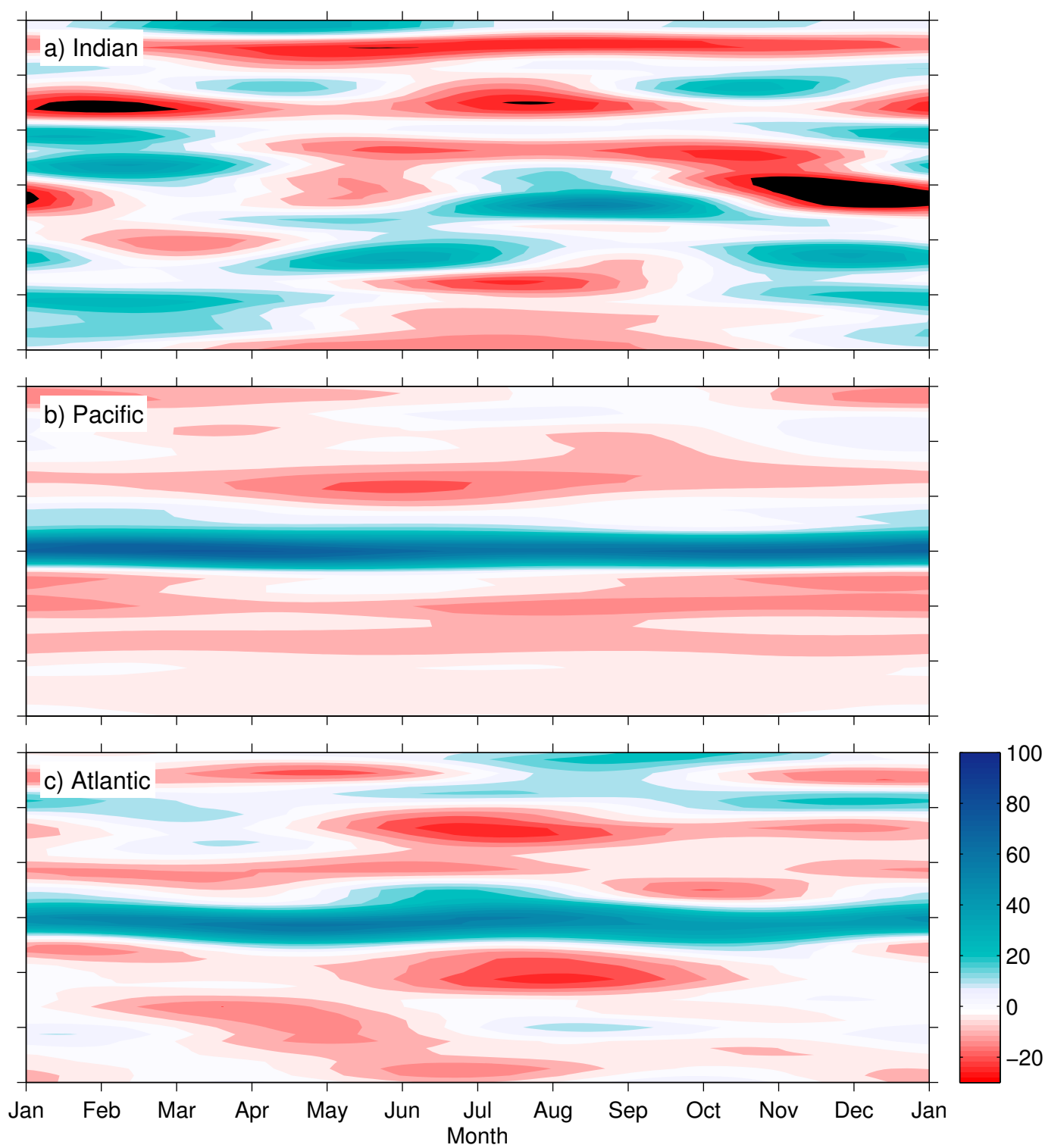


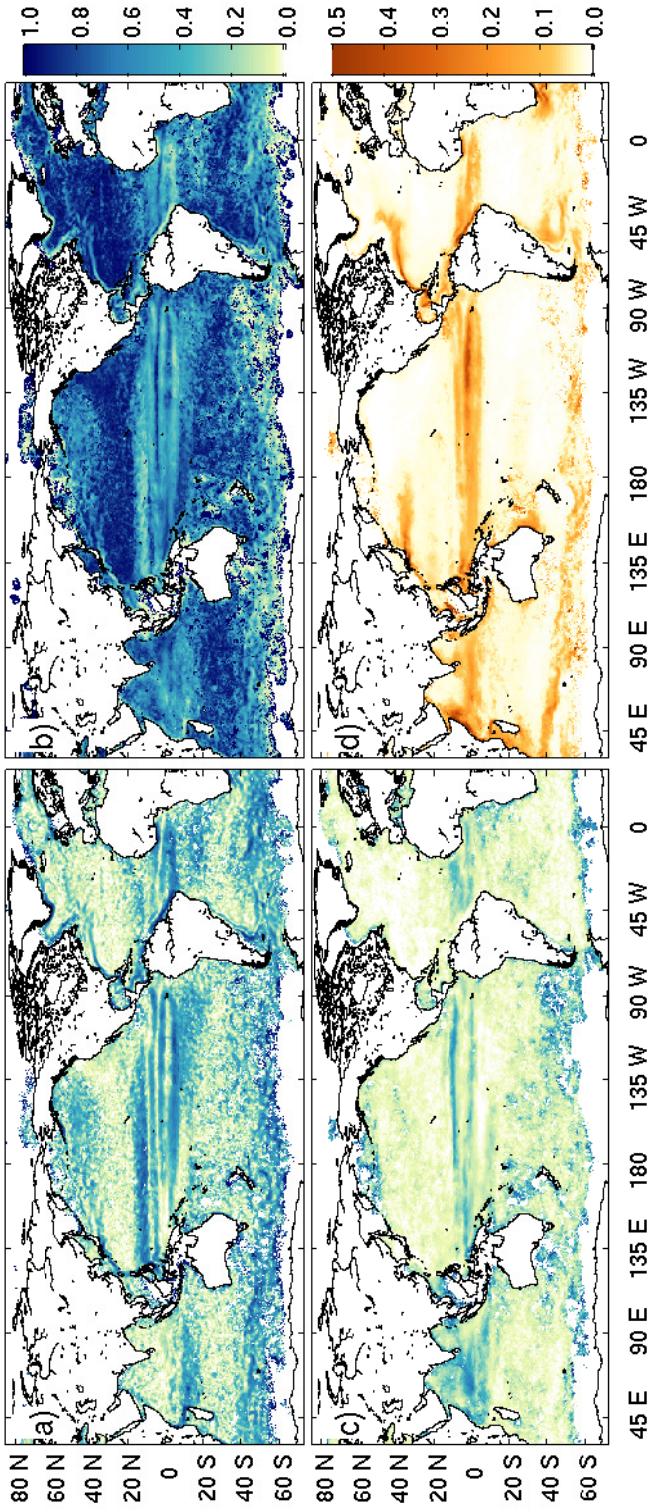
November

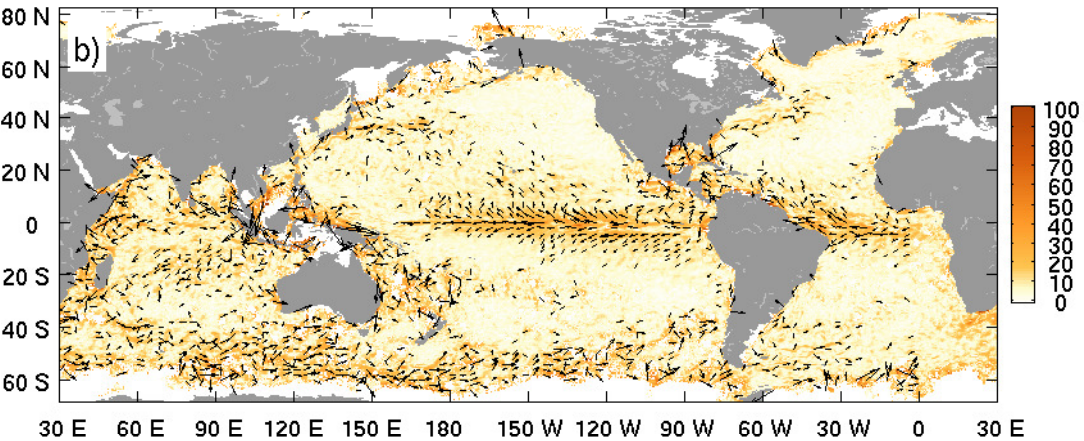
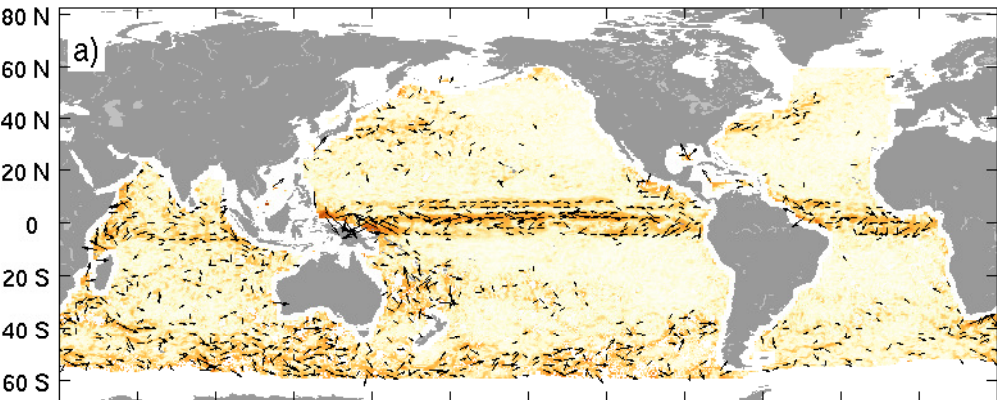


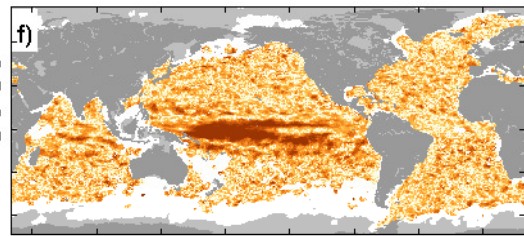
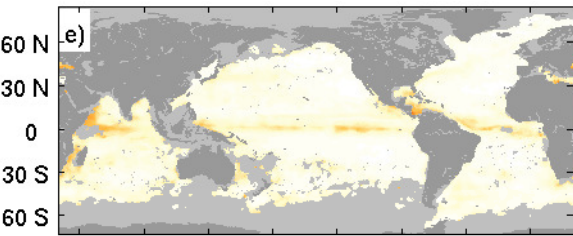
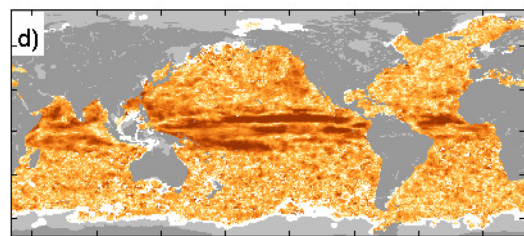
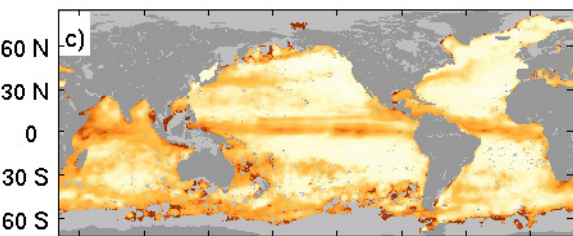
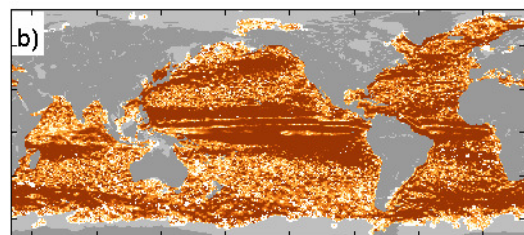
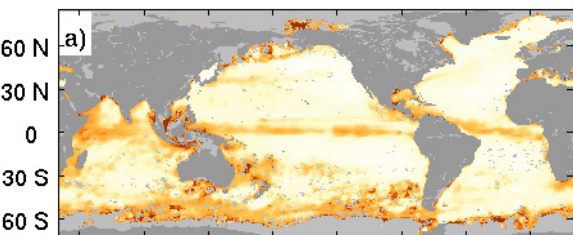
125 E 130 E 135 E 140 E 145 E

125 E 130 E 135 E 140 E 145 E









45 E 90 E 135 E 180 135 W 90 W 45 W 0

45 E 90 E 135 E 180 135 W 90 W 45 W 0